Applied Mathematical Modelling 103 (2022) 824–853

Contents lists available at ScienceDirect

Applied Mathematical Modelling

journal homepage: www.elsevier.com/locate/apm

Upwind finite element-PML approximation of a novel linear potential model for free surface flows produced by a floating rigid body

A. Bermúdez [a,b,d], O. Crego [a,*], A. Prieto [c]

[a] Departamento de Matemática Aplicada, Universidade de Santiago de Compostela, Santiago de Compostela E-15782, Spain
[b] Instituto de Matemáticas (IMAT), Universidade de Santiago de Compostela, Santiago de Compostela E-15782, Spain
[c] CITIC, Department of Mathematics, Universidade da Coruña, Spain
[d] Instituto Tecnológico de Matemática Industrial (ITMATI), Santiago de Compostela E-15782, Spain

ARTICLE INFO

Article history:
Received 26 March 2021
Revised 2 November 2021
Accepted 8 November 2021
Available online 17 November 2021

Keywords:
Linear potential model
Free surface
Kelvin wakes
Perfectly matched layer (PML)
Galerkin finite element method
Upwinding

ABSTRACT

A novel linear potential model is presented to compute free surface flows of incompressible fluids produced by the motion of a floating rigid body in the presence of an underlying non-uniform flow. In particular, the proposed model enables the accurate numerical simulation of the Kelvin wake pattern in a computational domain of reduced size. The governing equations are obtained by using an Arbitrary Lagrangian Eulerian (ALE) formulation which involves the underlying velocity of the fluid around the floating body assuming flat free surface, and a non-dimensional analysis to derive the novel linear system of equations for free surface flows. The discretization of the proposed model is made by a standard Galerkin finite element method, where a SUPG-inspired upwinding strategy has been used in combination with a Perfectly Matched Layer technique which allows truncating the original unbounded fluid domain without introducing spurious reflections in the Kelvin wake pattern. The numerical simulations computed with the proposed approach are compared with the results obtained by the classical linear potential model with uniform underlying flow and also with those from the full incompressible Navier–Stokes equations equipped with the $k-\omega$ SST turbulent model. This numerical comparison is discussed in terms of a classical hydrodynamic floating body benchmark involving the Wigley hull.

1. Introduction

The applications of hydrodynamics to naval architecture acquired increasing importance since the 1970s (see for instance, the classical textbook by Newman [1]). In this context, mathematical models based on the theory of potential flow have been widely utilized for the study of ship motions and the wave patterns generated by floating bodies. The purpose of this work is the derivation and numerical simulation of a novel linear potential model, which governs the propagation of the free surface waves generated by a moving floating body in the presence of an additional underlying fluid stream.

* Corresponding author.
E-mail addresses: alfredo.bermudez@usc.es (A. Bermúdez), oscar.crego@usc.es (O. Crego), andres.prieto@udc.es (A. Prieto).

https://doi.org/10.1016/j.apm.2021.11.004

Nomenclature

a	subscript denotes functions in AL coordinates
m	subscript denotes functions in material coordinates
$\hat{}$	denotes functions defined in the PML domain
$\tilde{}$	denotes non-dimensional expressions
$p = (p_1, p_2, p_3)$	material coordinates
$x = (x_1, x_2, x_3)$	Eulerian coordinates
$z = (z_1, z_2, z_3)$	AL coordinates
$\{\mathbf{g}_1, \mathbf{g}_2, \mathbf{g}_3\}$	basis of the reference frame in AL coordinates
$\mathbf{b}$	external body forces
$\mathbf{d}$	underlying velocity
g	gravitational acceleration
h_d	mesh tetrahedron diameter
k	upwinding function
$\mathbf{n}$	outward unit normal vector to $\partial\mathcal{A}_t$
$\mathbf{n}_a$	outward unit normal vector to $\partial\mathcal{A}$ and $\partial\mathcal{A}_F$
$\mathbf{n}_\infty$	outward unit normal vector to $\partial\mathcal{A}_\infty$
o	origin of the reference frame in Eulerian coordinates
t	time
$\mathbf{u}$	displacement of motion Y_f
$\mathbf{v}$	material velocity in Eulerian coordinates
$\mathbf{v}^{ap}$	apparent velocity in AL coordinates
$\mathbf{v}^r$	ship velocity in Eulerian coordinates
$\mathbf{v}^s$	stream velocity in Eulerian coordinates
B_w, L_w, D_w	main dimensions of the hull at midship (beam, waterline length and draft, respectively)
Fr	Froude number
$\mathbf{F}_{Y_f}$	gradient of Y_f in AL coordinates
H, L, V	typical values of height, length and velocity used to get dimensionless variables
$\mathbf{I}$	identity tensor
P_{X_f}, P_{Y_f}, P_{Z_f}	reference mappings of motions X_f, Y_f and Z_f
R, R_∞	inner and outer radius of the annular PML domain
$\mathbf{S}$, $\mathbf{C}$	PML tensors (see Sect. 6.2)
$\mathcal{T}$	trajectory of motion X_f
$\mathbf{T}$	Cauchy stress tensor
X_f	motion of the fluid
Y_f	motion perturbation defined in AL configuration
η_a	vertical component of Y_f
Z_f	underlying motion
β	auxiliary variable for upwinding
γ, $\hat{\gamma}$, $\hat{r}$, σ_θ	PML functions
δ_{SUPG}	SUPG constant
η	free surface elevation in Eulerian coordinates
π	pressure in Eulerian coordinates
ρ_f	mass density of the fluid
σ_r	radial PML absorption profile
φ	velocity potential in Eulerian coordinates
ϕ_a	velocity potential perturbation in AL coordinates
(r, θ, z)	cylindrical coordinates in AL configuration

Domain nomenclature

Ω	material (or Lagrangian) domain
$\mathcal{A}_t$	fluid domain in Eulerian coordinates
Γ_t^f, Γ_t^r, Γ_t^b	free surface, wet surface and seabed boundaries in Eulerian coordinates
$\mathcal{A}$	fluid domain in AL coordinates
Γ_a^f, Γ_a^r, Γ_a^b	free surface, wet surface and seabed boundaries in AL coordinates
$\mathcal{A}_F$	truncated fluid domain
$\partial\mathcal{A}^f$, $\partial\mathcal{A}^r$, $\partial\mathcal{A}^b$	free surface, wet surface and seabed boundaries in the truncated domain
$\partial\mathcal{A}^i$	inner boundary between the fluid and the PML domains

$\mathcal{A}_\infty$	PML domain
$\partial\mathcal{A}^f_\infty$, $\partial\mathcal{A}^b_\infty$, $\partial\mathcal{A}^\infty$	free surface, seabed and outer boundaries of the PML domain

Recently, the increase of computational resources has allowed to solve numerically more complex hydrodynamic models such as the Reynolds-averaged Navier–Stokes equations (see Kinaci et al. [2]). However, accurate numerical approximations of these models are computationally demanding. Consequently, simplified models, Kuznetsov et al. [3], are often used in the early stages of ship design, since they are suitable for quick (although may be less accurate) computations obtained in a feasible time. In this work as in many others, the Navier–Stokes equations are simplified into the Bernoulli and Laplace equations assuming irrotational flow of an incompressible and inviscid fluid.

This manuscript presents a rigorous approach using an Arbitrary Lagrangian–Eulerian (ALE) formulation together with a linearization to obtain a novel linear potential model. In the case of unsteady flow phenomena, the description of their governing equations using a Lagrangian or an ALE framework enables to work in a fixed (i.e., time independent) computational domain (see, for instance, some applications to the Navier–Stokes equations in Sarrate et al. [4], Benítez and Bermúdez [5]). In previous works, linear models similar to but different from the one proposed in this document (see for instance [6–8]) have been deduced using formal arguments rather than a rigorous mathematical justification (see Sections 3 and 4).

An important feature of the faced problem is that the free surface perturbation associated with the body motion can be propagated far from their source (see Fig. 1), which can represent a drawback when the original unbounded fluid domain is truncated for discretization purposes. Currently, the Perfectly Matched Layer (PML) is a standard technique to model wave propagation phenomena in unbounded domains, in such a way that the computational domain of interest is surrounded by an absorbing artificial layer, which does not introduce any spurious reflections in the solution of the original problem. It was first proposed by Berenger [9] for electromagnetic problems but it is also widely used in other fields as acoustics (see Abarbanel et al. [10], Qi and Geers [11], Bermúdez et al. [12]), or linearised water waves (see Cohen and Imperiale [13]). In the present approach the two-dimensional Cartesian PML model has been extended to three dimensions in cylindrical coordinates with the aim of absorbing the outgoing wave pattern generating by the floating body (i.e., the Kelvin wake) and preserving the structure of the convected terms presented in the free boundary condition.

Moreover, in the 1980s, the Streamline Upwind Petrov–Galerkin (SUPG) method was introduced in Brooks and Hughes [14] for upwinding the convective term in convection dominated flows. The SUPG method can be understood as a stabilization technique (see, for instance, Giuliani et al. [8], Pironneau [15], Mola et al. [16]) for standard finite element discretizations. In order to deal with the convective term involved in the free surface boundary condition, the SUPG method must be applied both in the fluid and in the PML governing equations without introducing numerical artifacts in the discrete solutions. With this purpose, a novel SUPG-inspired upwind strategy has been considered, ensuring the compatibility and the accuracy of the upwinding approach with the free surface boundary in the fluid and PML domains.

The structure of the present manuscript is described as follows: First, the motion equation and the constitutive laws for an incompressible and inviscid fluid are described in Eulerian coordinates in Section 2. Then, an Arbitrary Lagrangian–Eulerian formulation of the fluid governing equations is written in Section 3, which is then linearised in Section 4. Afterwards, the corresponding steady state model is introduced in Section 5 to complete the modelling part of this manuscript. Section 6 is focused on the discrete procedure used to solve the proposed model: a standard piecewise linear finite element method in combination with the above mentioned SUPG-inspired upwinding method and the PML technique. Then, in Section 7 the numerical results obtained with the proposed approach are validated under two different perspectives: First, they are compared with respect to the experimental data available in the classical Wigley hull benchmark (see Kajitani

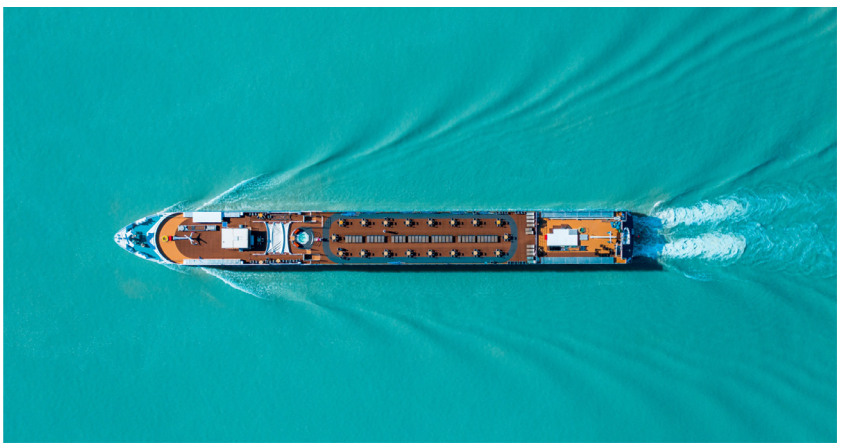

Fig. 1. Kelvin wake pattern generated by a cruise ship.

et al. [17]). Second, the numerical results of the present approach are analysed in comparison with those obtained with a full discretization of the unsteady Navier–Stokes equations equipped with the $k-\omega$ SST turbulent model. Finally, Section 8 collects the most relevant conclusions.

2. Model in Eulerian coordinates

Firstly, the governing equations of the motion of an incompressible and inviscid fluid with a free surface are described in Eulerian coordinates. With this purpose, some preliminary concepts on continuum mechanics will be recalled. Let $X_f : \Omega \times \mathbb{R}^+ \to \mathcal{A}_t$ be the motion of a fluid past a floating body such that, for each time t, $X_f(\cdot,t)$ is a deformation of the reference (material) configuration, Ω, into the region of the affine space occupied by the fluid at time t, $\mathcal{A}_t$, called spatial or Eulerian configuration at time t (see, for instance, Gurtin [18][1]). The trajectory of the motion is the set $\mathcal{T} := \{(x,t) : x \in \mathcal{A}_t, t > 0\}$ and the so-called reference map of the motion, $P_{X_f} : \mathcal{T} \to \Omega$, is defined by $P_{X_f}(\cdot,t) := (X(\cdot,t))^{-1}$. Finally, the Eulerian description of the material velocity, this is, the time derivative of the motion written in Eulerian coordinates is given by $\mathbf{v}(x,t) := \dfrac{\partial X_f}{\partial t}(p,t)\Big|_{p=P_{X_f}(x,t)}$.

Under the classical Cauchy's hypothesis in continuum mechanics, the non-conservative form of the motion equation written in Eulerian coordinates is given by

$$\rho_f \dot{\mathbf{v}} = \operatorname{div}\mathbf{T} + \mathbf{b} \quad \text{in } \mathcal{A}_t,\ t > 0,$$

where $\mathbf{T}$ is the Cauchy stress tensor, $\mathbf{b}$ is the external body force density and ρ_f is the mass density of the fluid, which is assumed constant. Since the fluid is considered incompressible and inviscid, it holds

$$\operatorname{div}\mathbf{v} = 0, \quad \mathbf{T} = -\pi\mathbf{I},$$

where π denotes the pressure field. Besides, the body force will be only driven by the gravity effects, so $\mathbf{b}(x,t) = \operatorname{grad}(-\rho_f g x_3)$. Thus, collecting the equations written above, the motion equation becomes

$$\rho_f \dot{\mathbf{v}} + \operatorname{grad}\pi = \operatorname{grad}(-\rho_f g x_3) \quad \text{in } \mathcal{A}_t,\ t > 0. \tag{1}$$

Since all domains $\mathcal{A}_t$ are assumed to be simply connected, which is a plausible assumption for both floating or submerged body in three spatial dimensions, then the flow is shown to be potential, i.e., there exists a scalar field $\varphi : \mathcal{T} \to \mathbb{R}$ such that $\mathbf{v} = \operatorname{grad}\varphi$. Consequently, the incompressibility condition and (1) can be written in terms of the velocity potential:

$$\begin{cases} \Delta\varphi = 0 & \text{in } \mathcal{A}_t,\ t > 0, \\ \rho_f (\operatorname{grad}\varphi)^{\cdot} + \operatorname{grad}\pi = \operatorname{grad}(-\rho_f g x_3) & \text{in } \mathcal{A}_t,\ t > 0. \end{cases} \tag{2}$$

Now, boundary conditions must be introduced to complete the mathematical model. The boundary of the unbounded fluid domain is split in three disjoint parts: the free boundary (on the top) of the fluid domain, Γ_t^f, the wet boundary of a floating (or submerged) body, Γ_t^r, and the bottom boundary of the fluid domain, Γ_t^b. Since the fluid is supposed to be inviscid, the normal velocity has to be continuous with respect to the imposed velocity of the floating body as it is assumed to be impervious. Thus, the boundary condition can be written as

$$\frac{\partial\varphi}{\partial\mathbf{n}} = \mathbf{v}^r \cdot \mathbf{n} \quad \text{on } \Gamma_t^r,\ t > 0, \tag{3}$$

where $\mathbf{v}^r$ denotes the possibly time-dependent velocity field of the rigid body. Analogously, on the rigid bottom surface, Γ_t^b, it holds

$$\frac{\partial\varphi}{\partial\mathbf{n}} = 0 \quad \text{on } \Gamma_t^b,\ t > 0. \tag{4}$$

These boundary conditions need to be complemented with an appropriate radiation condition at $|x-o| \to \infty$. Assuming the velocity field is constant at infinity, the radiation condition imposes that

$$\operatorname{grad}\varphi = \mathbf{v}^s \quad \text{for } |x-o| \to \infty,\ t > 0, \tag{5}$$

being $\mathbf{v}^s$ the constant stream velocity and o the origin in the Eulerian coordinate system.

The hydrodynamic model written above has to be completed by including two boundary conditions associated with the free boundary, as well as adequate initial conditions. The kinetic condition on the fluid free surface models the balance of forces by means of the Bernoulli equation, whereas the kinematic condition reflects the fact that a particle on the free surface, Γ_t^f, remains there at any time $t > 0$. The precise description of these two boundary conditions is postponed and they will be introduced once the model (2)–(5) has been written in the AL configuration.

[1] In [18] an introduction to the continuum mechanics framework can be found; the notations in this book will be followed throughout this article

3. Arbitrary Lagrangian–Eulerian model

To achieve a more tractable model where the physical domain of the hydrodynamic problem does not depend on time, an ALE formulation is used. With this purpose, the motion of the fluid $X_f : \Omega \times \mathbb{R}^+ \to \mathcal{A}_t$ is given as the composition of two mappings (see Fig. 2), $Y_f : \mathcal{A} \times \mathbb{R}^+ \to \mathcal{A}_t$ and $Z_f : \Omega \times \mathbb{R}^+ \to \mathcal{A}$, as follows:

$$X_f(p,t) = Y_f(Z_f(p,t),t). \tag{6}$$

Thus, on the one hand Z_f is identified as an underlying motion that determines the Arbitrary Lagrangian (AL) configuration. More precisely, the Eulerian (with respect to Z_f) domain occupied by the fluid in the underlying motion is fixed in time, namely, $Z_f(\Omega,t) = \mathcal{A}$, and it will be taken as the AL configuration. Therefore, this assumption implies the fixed free surface of the fluid domain in the AL configuration is not being perturbed by the underlying motion. For the sake of completeness, the ALE model is developed in Section 3.1. On the other hand, motion Y_f is identified as a small perturbation from the underlying motion Z_f. Consequently, the Kelvin wake pattern is obtained in the ALE formulation as the free surface elevation associated with Y_f.

Now, the Eulerian potential model (2)–(5) stated in terms of the motion X_f is rewritten in the AL configuration. For this purpose, it is necessary to introduce some notations. The velocity of the underlying flow is denoted by $\mathbf{d}(p,t) := \dfrac{\partial Z_f}{\partial t}(p,t)$ and $\mathbf{F}_{Y_f}(z,t) := \mathbf{grad}_a\, Y_f(z,t)$ denotes the deformation gradient of motion Y_f, where $\mathbf{grad}_a$ (respectively, grad_a) denotes the gradient of a vector field (respectively, a scalar field) defined in the AL configuration with respect to variable z. Besides, for a spatial field $f : \mathcal{T} \to \mathbb{R}$ and a material field $h : \Omega \times \mathbb{R}^+ \to \mathbb{R}$, the subscript a denotes their respective AL descriptions, namely,

$$f_a(z,t) = f\big(Y_f(z,t),t\big) \quad \text{and} \quad h_a(z,t) = h\big(P_{Z_f}(z,t),t\big) = h\big(P_{X_f}\big(Y_f(z,t),t\big),t\big),$$

where $P_{Z_f}(\cdot,t) := \big[Z_f(\cdot,t)\big]^{-1}$ is the reference mapping of motion Z_f. Analogously, the reference mapping associated with Y_f is defined as $P_{Y_f}(\cdot,t) = \big[Y_f(\cdot,t)\big]^{-1}$.

A straightforward application of an adequate change of variables on the model (2)–(5) leads to the following result:

Lemma 3.1. *Let φ be a solution of model (2)–(5), which is the potential velocity field associated with motion X_f. If Y_f, Z_f, and X_f are motions satisfying (6), and $\mathbf{F}_{Y_f}$, $\mathbf{F}_{Z_f}$ and $\mathbf{F}_{X_f}$ are their corresponding gradients then it holds*

$$\begin{aligned}
&(\Delta\varphi)_a = \mathrm{div}_a\left(\det(\mathbf{F}_{Y_f})\mathbf{F}_{Y_f}^{-1}\mathbf{F}_{Y_f}^{-t}\,\mathrm{grad}_a\,\varphi_a\right) = 0 && \text{in } \mathcal{A}\times\mathbb{R}^+,\\
&\frac{\partial Y_f}{\partial t} = \mathbf{F}_{Y_f}^{-t}\,\mathrm{grad}_a\,\varphi_a - \mathbf{F}_{Y_f}\mathbf{d}_a && \text{in } \mathcal{A}\times\mathbb{R}^+,\\
&\mathbf{F}_{Y_f}^{-1}\mathbf{F}_{Y_f}^{-t}\,\mathrm{grad}_a\,\varphi_a\cdot\mathbf{n}_a = \mathbf{F}_{Y_f}^{-1}\mathbf{v}_a^r\cdot\mathbf{n}_a && \text{on } \Gamma_a^r\times\mathbb{R}^+,\\
&\mathbf{F}_{Y_f}^{-1}\mathbf{F}_{Y_f}^{-t}\,\mathrm{grad}_a\,\varphi_a\cdot\mathbf{n}_a = 0 && \text{on } \Gamma_a^b\times\mathbb{R}^+,\\
&\mathbf{F}_{Y_f}^{-t}\,\mathrm{grad}\,\varphi_a = \mathbf{v}_a^s && \text{for } |z-o_a|\to\infty,\ t>0.
\end{aligned}$$

In order to write the boundary conditions imposed on the free boundary of the fluid domain, the balance of pressures and loads should be considered. More precisely, a version of the Bernoulli's theorem in the AL configuration is obtained (see its proof in Appendix A).

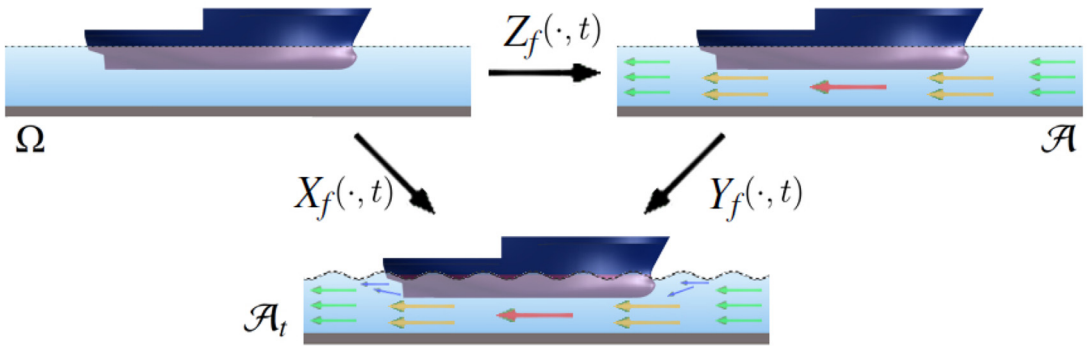

Fig. 2. ALE mapping diagram among the different configurations. $X_f(\cdot,t)$ is the total motion at time t. $Z_f(\cdot,t)$ and $Y_f(\cdot,t)$ are respectively the underlying motion and its perturbation at time t. Coloured arrows highlight the underlying velocity field in the AL configuration domain, $\mathcal{A}$, and the velocity field in the spatial configuration domain at time t, $\mathcal{A}_t$.

Theorem 3.1 (Bernoulli equation in AL coordinates)**.** *Under the same hypothesis of Lemma 3.1, the following equality holds:*

$$-\rho_f\left(\left(\mathbf{grad}_a\,\frac{\partial \mathbf{u}}{\partial t}\right)^t+(\mathbf{grad}_a(\mathbf{grad}_a\,\mathbf{u})^t)\mathbf{d}_a\right)\mathbf{F}_{Y_f}^{-t}\,\mathrm{grad}_a\,\varphi_a+\rho_f\,\mathbf{grad}_a\,\mathrm{grad}_a\,\varphi_a\mathbf{d}_a+\mathrm{grad}_a\left(\rho_f\frac{\partial\varphi_a}{\partial t}+\pi_a+\rho_f g\eta_a\right)=\mathbf{0}\quad\text{in } \mathcal{A}\times\mathbb{R}^+,$$

where $\eta_a(z,t)=(Y_f(z,t)-o_a)\cdot\mathbf{g}_3$ is the third coordinate of motion Y_f and $\mathbf{u}(z,t)=Y_f(z,t)-z$ is the displacement field of motion Y_f.

Thus, collecting the results of Lemma 3.1 and Theorem 3.1, the hydrodynamic model (2)–(5) written in the AL configuration is given by

$$\begin{cases}
\mathrm{div}_a\left(\det(\mathbf{F}_{Y_f})\mathbf{F}_{Y_f}^{-1}\mathbf{F}_{Y_f}^{-t}\,\mathrm{grad}_a\,\varphi_a\right)=0 & \text{in } \mathcal{A}\times\mathbb{R}^+,\\
\dfrac{\partial Y_f}{\partial t}=\mathbf{F}_{Y_f}^{-t}\,\mathrm{grad}_a\,\varphi_a-\mathbf{F}_{Y_f}\mathbf{d}_a & \text{in } \mathcal{A}\times\mathbb{R}^+,\\
-\rho_f\left(\left(\mathbf{grad}_a\,\dfrac{\partial \mathbf{u}}{\partial t}\right)^t+(\mathbf{grad}_a(\mathbf{grad}_a\,\mathbf{u})^t)\mathbf{d}_a\right)\mathbf{F}_{Y_f}^{-t}\,\mathrm{grad}_a\,\varphi_a+\rho_f\,\mathbf{grad}_a\,\mathrm{grad}_a\,\varphi_a\mathbf{d}_a & \\
+\mathrm{grad}_a\left(\rho_f\dfrac{\partial\varphi_a}{\partial t}+\pi_a+\rho_f g\eta_a\right)=\mathbf{0} & \text{in } \mathcal{A}\times\mathbb{R}^+,\\
\mathbf{F}_{Y_f}^{-1}\mathbf{F}_{Y_f}^{-t}\,\mathrm{grad}_a\,\varphi_a\cdot\mathbf{n}_a=\mathbf{F}_{Y_f}^{-1}\mathbf{v}_a^r\cdot\mathbf{n}_a & \text{on } \Gamma_a^r\times\mathbb{R}^+,\\
\mathbf{F}_{Y_f}^{-1}\mathbf{F}_{Y_f}^{-t}\,\mathrm{grad}_a\,\varphi_a\cdot\mathbf{n}_a=0 & \text{on } \Gamma_a^b\times\mathbb{R}^+,\\
\mathbf{F}_{Y_f}^{-t}\,\mathrm{grad}_a\,\varphi_a=\mathbf{v}_a^s & \text{for } |z-o_a|\to\infty, t>0.
\end{cases}\tag{7}$$

3.1. The underlying motion

The hydrodynamic model (7) written in the AL configuration requires the a priori knowledge of the underlying velocity field $\mathbf{d}_a$, which is generated due to the ship motion (with a fixed velocity $\mathbf{v}^r$) and a fluid stream velocity (with a fixed velocity $\mathbf{v}^s$). To compute this underlying flow, the (Eulerian with respect to Z_f) domain with flat surface, $\mathcal{A}$, is considered. As it has been mentioned above, this domain is also assumed as the Arbitrary Lagrangian (AL) configuration for the perturbed flow Y_f. Under the same hypothesis of incompressibility and non-viscosity of the fluid, the underlying flow is also assumed potential, this is, $\mathbf{d}_a=\mathrm{grad}_a\,\varphi_0$. Since the velocity field $\mathbf{d}_a$ is tangent to the flat free surface, the potential field satisfies (see, for instance, Landau and Lifshitz [19])

$$\begin{cases}
\Delta_a\varphi_0=0 & \text{in } \mathcal{A},\\
\dfrac{\partial\varphi_0}{\partial\mathbf{n}_a}=0 & \text{on } \Gamma_a^f\cup\Gamma_a^b,\\
\dfrac{\partial\varphi_0}{\partial\mathbf{n}_a}=\mathbf{v}_a^r\cdot\mathbf{n}_a & \text{on } \Gamma_a^r,\\
\mathrm{grad}_a\,\varphi_0=\mathbf{v}_a^s & \text{for } |z-o_a|\to\infty,
\end{cases}\tag{8}$$

where recall that $\mathbf{v}_a^r$ is the ship velocity and $\mathbf{v}_a^s$ is the stream velocity. Notice that φ_0 is the so-called *double-body potential* (see, for instance, Shahjada Tarafder and Suzuki [6]).

The potential field φ_0 is decomposed by using the stream velocity as $\varphi_0=\mathbf{v}_a^s\cdot(z-o_a)+\phi_0$. Hence, the model can be rewritten in terms of the potential ϕ_0, the stream velocity $\mathbf{v}_a^s$, and the apparent velocity, $\mathbf{v}^{ap}=\mathbf{v}_a^s-\mathbf{v}_a^r$ as follows:

$$\begin{cases}
\Delta_a\phi_0=0 & \text{in } \mathcal{A},\\
\dfrac{\partial\phi_0}{\partial\mathbf{n}_a}=0 & \text{on } \Gamma_a^f,\\
\dfrac{\partial\phi_0}{\partial\mathbf{n}_a}=-\mathbf{v}_a^s\cdot\mathbf{n}_a & \text{on } \Gamma_a^b,\\
\dfrac{\partial\phi_0}{\partial\mathbf{n}_a}=-\mathbf{v}^{ap}\cdot\mathbf{n}_a & \text{on } \Gamma_a^r,\\
\mathrm{grad}_a\,\phi_0=\mathbf{0} & \text{for } |z-o_a|\to\infty.
\end{cases}\tag{9}$$

Consequently, the underlying velocity is

$$\mathbf{d}_a=\mathrm{grad}_a\,\varphi_0=\mathrm{grad}_a\,\phi_0+\mathbf{v}_a^s.$$

Notice that problem (9) does not involve any convective term and therefore an accurate discretization of this problem does not require any upwinding method. Moreover, in absence of transport phenomena in this model, the decay of the Laplacian solution ϕ_0 avoids the use of large computational domains. Indeed, it has been numerically verified that truncating the domain without any damping methodology does not introduce significant numerical errors, even in the case where this truncation is done at a small finite distance of the floating body.

4. Linear approximation

Since the motion X_f has been assumed as a small perturbation Y_f from the underlying motion Z_f, a linear model can be used to approximate the velocity potential φ_a. Associated with Y_f in (7), the linear model is obtained by applying a dimensional analysis to the equations in (7) and keeping only the first order terms with respect to a small parameter.

The typical value of the displacement perturbation (which is closely related with the magnitude of the oscillations of the free surface of the fluid) and the length of the floating body are denoted by H and L, respectively. Besides, the typical value of the apparent velocity of the underlying motion (more precisely, the subtraction of the stream and the rigid floating body velocities) is denoted by V. Then, L/V is the typical time the fluid takes to travel along the floating body. Accordingly, the following non-dimensional variables are introduced:

$$\tilde{t} = \frac{V}{L}t, \qquad \tilde{z} - o_a = \frac{1}{L}(z - o_a), \qquad \tilde{\mathbf{v}}_a^r = \frac{1}{V}\mathbf{v}_a^r, \qquad \tilde{\mathbf{v}}_a^s = \frac{1}{V}\mathbf{v}_a^s, \qquad \tilde{\eta}_a = \frac{1}{L}\eta_a,$$
$$\tilde{\mathbf{d}}_a = \frac{1}{V}\mathbf{d}_a, \quad \tilde{\mathbf{u}} = \frac{1}{H}\mathbf{u}, \qquad \tilde{\varphi}_a = \frac{1}{VL}\varphi_a, \quad \tilde{\pi}_a = \frac{L}{\rho_f V^2 L}\pi_a.$$

Hence, once the second equation of model (7) is rewritten in terms of the displacement $\mathbf{u}$ (notice $\frac{\partial Y_f}{\partial t} = \frac{\partial \mathbf{u}}{\partial t}$) the non-dimensional version of (7) is given by

$$\begin{cases}
\widetilde{\mathrm{div}}_a\Big(\det(\tilde{\mathbf{F}}_{Y_f})\tilde{\mathbf{F}}_{Y_f}^{-1}\tilde{\mathbf{F}}_{Y_f}^{-t}\widetilde{\mathrm{grad}}_a\tilde{\varphi}_a\Big) = 0 & \text{in } \tilde{\mathcal{A}}\times\mathbb{R}^+,\\
\dfrac{VH}{L}\dfrac{\partial\tilde{\mathbf{u}}}{\partial\tilde{t}} = V\tilde{\mathbf{F}}_{Y_f}^{-t}\widetilde{\mathrm{grad}}_a\tilde{\varphi}_a - V\tilde{\mathbf{F}}_{Y_f}\tilde{\mathbf{d}}_a & \text{in } \tilde{\mathcal{A}}\times\mathbb{R}^+,\\
-V\rho_f\left(\dfrac{VH}{L^2}\left(\widetilde{\mathbf{grad}}_a\dfrac{\partial\tilde{\mathbf{u}}}{\partial\tilde{t}}\right)^t + \dfrac{VH}{L^2}(\widetilde{\mathbf{grad}}_a(\widetilde{\mathbf{grad}}_a\tilde{\mathbf{u}})^t)\tilde{\mathbf{d}}_a\right)\tilde{\mathbf{F}}_{Y_f}^{-t}\widetilde{\mathrm{grad}}_a\tilde{\varphi}_a & \\
+\dfrac{V^2}{L}\rho_f\widetilde{\mathbf{grad}}_a\widetilde{\mathrm{grad}}_a\tilde{\varphi}_a\tilde{\mathbf{d}}_a + \dfrac{1}{L}\widetilde{\mathrm{grad}}_a\left(V^2\rho_f\dfrac{\partial\tilde{\varphi}_a}{\partial\tilde{t}} + V^2\rho_f\tilde{\pi}_a + L\rho_f g\tilde{\eta}_a\right) = \mathbf{0} & \text{in } \tilde{\mathcal{A}}\times\mathbb{R}^+,\\
V\tilde{\mathbf{F}}_{Y_f}^{-1}\tilde{\mathbf{F}}_{Y_f}^{-t}\widetilde{\mathrm{grad}}_a\tilde{\varphi}_a\cdot\tilde{\mathbf{n}}_a = V\tilde{\mathbf{F}}_{Y_f}^{-1}\tilde{\mathbf{v}}_a^r\cdot\tilde{\mathbf{n}}_a & \text{on } \tilde{\Gamma}_a^r\times\mathbb{R}^+,\\
V\tilde{\mathbf{F}}_{Y_f}^{-1}\tilde{\mathbf{F}}_{Y_f}^{-t}\widetilde{\mathrm{grad}}_a\tilde{\varphi}_a\cdot\tilde{\mathbf{n}}_a = 0 & \text{on } \tilde{\Gamma}_a^b\times\mathbb{R}^+,\\
V\tilde{\mathbf{F}}_{Y_f}^{-t}\widetilde{\mathrm{grad}}_a\tilde{\varphi}_a = V\tilde{\mathbf{v}}_a^s & \text{for } |\tilde{z}-o_a|\to\infty,\ \tilde{t}>0,
\end{cases} \tag{10}$$

where $\tilde{\ }$ denotes non-dimensional differential operators and fields. Since $H \ll L$ in typical naval architecture applications (see [1]), it is assumed that $\epsilon = \dfrac{H}{L}$ is a small parameter. Consequently, the tensor field $\tilde{\mathbf{F}}_{Y_f} = \mathbf{I} + \dfrac{H}{L}\widetilde{\mathbf{grad}}_a\tilde{\mathbf{u}}$ and the Bernoulli equation (third equation in (10)) can be rewritten as

$$\tilde{\mathbf{F}}_{Y_f} = \mathbf{I} + O(\epsilon)$$

and

$$\frac{V^2}{L}\left(\rho_f\widetilde{\mathbf{grad}}_a\widetilde{\mathrm{grad}}_a\tilde{\varphi}_a\tilde{\mathbf{d}}_a + \widetilde{\mathrm{grad}}_a\left(\rho_f\frac{\partial\tilde{\varphi}_a}{\partial\tilde{t}} + \rho_f\tilde{\pi}_a\right) + O(\epsilon)\right) + \widetilde{\mathrm{grad}}_a\big(\rho_f g\tilde{\eta}_a\big) = \mathbf{0},$$

respectively. Thus, the following linear approximations of the equations written above in their dimensional form are deduced:

$$\mathbf{F}_{Y_f} = \mathbf{I} \quad \text{in } \mathcal{A}\times\mathbb{R}^+, \tag{11}$$
$$\rho_f\mathbf{grad}_a\mathrm{grad}_a\varphi_a\mathbf{d}_a + \mathrm{grad}_a\big(\rho_f\tfrac{\partial\varphi_a}{\partial t} + \pi_a + \rho_f g\eta_a\big) = \mathbf{0} \quad \text{in } \mathcal{A}\times\mathbb{R}^+. \tag{12}$$

Now, taking into account the linear approximations (11) and (12), a linearised model can be written from (7). For this purpose, $\mathbf{F}_{Y_f}$ is approximated by $\mathbf{I}$ in (10) unless in the second term on the right-hand side of the second equation in (7). Notice that even if $\mathbf{F}_{Y_f}$ is kept there, the model will be linear. However, if any other occurrence of $\mathbf{F}_{Y_f}$ were kept then the model would be non-linear. In addition, notice that if $\mathbf{F}_{Y_f}$ were approximated by $\mathbf{I}$ in all occurrences then $\varphi_a = \varphi_0$ so the Kelvin wave pattern would not be a solution of the linear model derived from (10). As a consequence, the following linear approximate model is finally adopted:

$$\begin{cases}
\Delta_a\varphi_a = 0 & \text{in } \mathcal{A}\times\mathbb{R}^+,\\
\dfrac{\partial Y_f}{\partial t} = \mathrm{grad}_a\,\varphi_a - \mathbf{grad}_a\,Y_f\mathbf{d}_a & \text{in } \mathcal{A}\times\mathbb{R}^+,\\
\rho_f\,\mathbf{grad}_a\,\mathrm{grad}_a\,\varphi_a\mathbf{d}_a + \mathrm{grad}_a\left(\rho_f\dfrac{\partial\varphi_a}{\partial t} + \pi_a + \rho_f g\eta_a\right) = \mathbf{0} & \text{in } \mathcal{A}\times\mathbb{R}^+,\\
\dfrac{\partial\varphi_a}{\partial\mathbf{n}_a} = \mathbf{v}_a^r\cdot\mathbf{n}_a & \text{on } \Gamma_a^r\times\mathbb{R}^+,\\
\dfrac{\partial\varphi_a}{\partial\mathbf{n}_a} = 0 & \text{on } \Gamma_a^b\times\mathbb{R}^+,\\
\mathrm{grad}_a\,\varphi_a = \mathbf{v}_a^s & \text{for } |z-o_a|\to\infty\ t>0,
\end{cases} \tag{13}$$

where the velocity potential φ_a, pressure π_a and the motion Y_f are the unknown fields to be computed, whereas $\mathbf{d}_a$ is assumed to be known (recall that it is computed from the solution ϕ_0 of problem (9)). Notice that model (13) is overconstrained. In order to get a balanced model and reduce the unknowns only to the velocity potential φ_a, in the next section, some analytic computations are made previous to its numerical solution.

5. Steady state

Now, once the AL description of the time-dependent hydrodynamic problem has been introduced and linearized in the previous section, it will be solved at the steady state, as the main goal of this work consists in the numerical simulation of the Kelvin wakes and this phenomenon is steady in the proposed AL framework. Hence, considering that velocities $\mathbf{v}_a^s$ and $\mathbf{v}_a^r$ are time independent, the steady state model is deduced from (13) by suppressing the terms involving time derivatives. Unlike the classical hydrodynamic model (see Remark 5.1 below), the system of equations (13) also involves the vector unknown Y_f and the pressure π_a, in addition to the scalar unknown φ_a. In order to consider only one scalar unknown, the steady version of the second equation in (13) is multiplied by the outward unit normal vector to the free surface in the AL configuration (for simplicity, it is assumed to be the third vector of the standard Cartesian basis in the AL coordinate system, $\mathbf{g}_3$). Thus,

$$\mathbf{grad}_a Y_f \mathbf{d}_a \cdot \mathbf{g}_3 = \operatorname{grad}_a \varphi_a \cdot \mathbf{g}_3 \quad \text{in } \mathcal{A}$$

and since $\mathbf{grad}_a Y_f \mathbf{d}_a \cdot \mathbf{g}_3 = \mathbf{d}_a \cdot (\mathbf{grad}_a Y_f)^t \mathbf{g}_3 = \mathbf{d}_a \cdot \operatorname{grad}_a (Y_f \cdot \mathbf{g}_3)$, then

$$\operatorname{grad}_a \varphi_a \cdot \mathbf{g}_3 = \operatorname{grad}_a \eta_a \cdot \mathbf{d}_a \quad \text{in } \mathcal{A}. \tag{14}$$

Similarly, the steady version of the third equation of model (13) is scalarly multiplied by $\mathbf{d}_a$ to get

$$\rho_f \mathbf{grad}_a \operatorname{grad}_a \varphi_a \mathbf{d}_a \cdot \mathbf{d}_a + \operatorname{grad}_a (\pi_a + \rho_f g \eta_a) \cdot \mathbf{d}_a = 0 \quad \text{in } \mathcal{A}.$$

Taking into account (14) and the assumption of constant mass density of the fluid, it leads to

$$\rho_f \mathbf{grad}_a \operatorname{grad}_a \varphi_a \mathbf{d}_a \cdot \mathbf{d}_a + \operatorname{grad}_a \pi_a \cdot \mathbf{d}_a + \rho_f g \operatorname{grad}_a \varphi_a \cdot \mathbf{g}_3 = 0 \quad \text{in } \mathcal{A}. \tag{15}$$

On the free surface Γ_a^f, pressure π_a is supposed to be spatially homogeneous (usually equal to the atmospheric pressure). Since the outward unit normal vector to Γ_a^f is $\mathbf{n}_a = \mathbf{g}_3$ and $\mathbf{d}_a$ is tangent to the free surface then $\mathbf{d}_a \cdot \mathbf{g}_3 = 0$. Due to all the arguments described above, $\operatorname{grad}_a \pi_a \cdot \mathbf{d}_a = 0$ on Γ_a^f. Therefore, restricted to the free boundary, Eq. (15) yields the boundary condition

$$\frac{\partial \varphi_a}{\partial \mathbf{n}_a} = -\frac{1}{g} \mathbf{grad}_a \operatorname{grad}_a \varphi_a \mathbf{d}_a \cdot \mathbf{d}_a \text{ on } \Gamma_a^f.$$

Keeping in mind the radiation condition, the potential φ_a is decomposed using the same procedure applied to compute the underlying motion (see the decomposition for φ_0 described in Section 3) as $\varphi_a = \mathbf{v}_a^s \cdot (z - o_a) + \phi_a$. Thus, $\operatorname{grad}_a \phi_a = \operatorname{grad}_a \varphi_a - \mathbf{v}_a^s$ and the normal derivative of ϕ_a can be written in terms of φ_a as follows:

$$\frac{\partial \phi_a}{\partial \mathbf{n}_a} = \frac{\partial \varphi_a}{\partial \mathbf{n}_a} - \mathbf{v}_a^s \cdot \mathbf{n}_a.$$

Since $\mathbf{v}_a^s$ is tangent to the free surface boundary, then $\mathbf{v}_a^s \cdot \mathbf{n}_a = 0$ on Γ_a^f. Moreover, as it is spatially constant then

$$\frac{\partial \phi_a}{\partial \mathbf{n}_a} = -\frac{1}{g} \mathbf{grad}_a \operatorname{grad}_a \phi_a \mathbf{d}_a \cdot \mathbf{d}_a \quad \text{on } \Gamma_a^f.$$

Additionally, the equation written above is equivalent to

$$\frac{\partial \phi_a}{\partial \mathbf{n}_a} = -\frac{1}{g} \operatorname{grad}_a (\operatorname{grad}_a \phi_a \cdot \mathbf{d}_a) \cdot \mathbf{d}_a + \frac{1}{g} \operatorname{grad}_a \phi_a \cdot \mathbf{grad}_a \mathbf{d}_a \mathbf{d}_a \quad \text{on } \Gamma_a^f. \tag{16}$$

In conclusion, the AL formulation (13) for the steady-state becomes

$$\begin{cases} \Delta_a \phi_a = 0 & \text{in } \mathcal{A}, \\ \dfrac{\partial \phi_a}{\partial \mathbf{n}_a} = -\dfrac{1}{g} \operatorname{grad}_a (\operatorname{grad}_a \phi_a \cdot \mathbf{d}_a) \cdot \mathbf{d}_a + \dfrac{1}{g} \operatorname{grad}_a \phi_a \cdot \mathbf{grad}_a \mathbf{d}_a \mathbf{d}_a & \text{on } \Gamma_a^f, \\ \dfrac{\partial \phi_a}{\partial \mathbf{n}_a} = -\mathbf{v}^{ap} \cdot \mathbf{n}_a & \text{on } \Gamma_a^r, \\ \dfrac{\partial \phi_a}{\partial \mathbf{n}_a} = -\mathbf{v}_a^s \cdot \mathbf{n}_a & \text{on } \Gamma_a^b, \\ \operatorname{grad}_a \phi_a = \mathbf{0} & \text{for } |z - o_a| \to \infty, \end{cases} \tag{17}$$

where recall that $\mathbf{v}^{ap} = \mathbf{v}_a^s - \mathbf{v}_a^r$ is the apparent velocity of the fluid observed from the floating body.

Remark 5.1. Notice that the present model is a generalization of the classical one found in the bibliography (see, for instance, Newman [1]) which has been widely used to compute Kelvin wake patterns (see, for instance, Giuliani et al. [8]).

The difference with the model introduced in (17) lies in the free surface boundary condition. Indeed, since $\mathbf{v}^{ap}$ is constant in these references, replacing $\mathbf{d}_a$ by $\mathbf{v}^{ap}$ in the free boundary condition of (17) leads to

$$\begin{cases} \Delta_a \phi_a = 0 & \text{in } \mathcal{A} \\ \dfrac{\partial \phi_a}{\partial \mathbf{n}_a} = -\dfrac{1}{g}\,\mathrm{grad}_a(\mathrm{grad}_a\,\phi_a \cdot \mathbf{v}^{ap}) \cdot \mathbf{v}^{ap} & \text{on } \Gamma_a^f, \\ \dfrac{\partial \phi_a}{\partial \mathbf{n}_a} = -\mathbf{v}^{ap} \cdot \mathbf{n}_a & \text{on } \Gamma_a^r, \\ \dfrac{\partial \phi_a}{\partial \mathbf{n}_a} = -\mathbf{v}_a^s \cdot \mathbf{n}_a & \text{on } \Gamma_a^b, \\ \mathrm{grad}_a\,\phi_a = \mathbf{0} & \text{for } |z - o_a| \to \infty, \end{cases} \tag{18}$$

which is an equivalent writing of the classical linear model. Thus, the difference between (17) and (18) lies on the type of assumed underlying motion: $\mathbf{d}_a = \mathbf{v}^{ap}$ is constant in (18), but the underlying motion $\mathbf{d}_a$ used in (17) varies spatially since it comes from solving (9), this is, $\mathbf{d}_a = \mathrm{grad}_a\,\phi_0 + \mathbf{v}_a^s$. □

From a weak formulation point of view, model (17) could lead to an ill-posed variational problem stated in standard Sobolev spaces, as it involves a second order differential operator applied on the free surface Γ_a^f. However, since $\mathbf{d}_a$ is a tangential vector to Γ_a^f, the trace $\mathrm{grad}_a\,\phi_a \cdot \mathbf{d}_a$ can be defined for $\phi_a \in H^1(\mathcal{A})$ and an analogous argument could be applied to $\mathrm{grad}_a(\mathrm{grad}_a\,\phi_a \cdot \mathbf{d}_a) \cdot \mathbf{d}_a$ as far as $\mathrm{grad}_a\,\phi_a \cdot \mathbf{d}_a \in H^1(\mathcal{A})$. Moreover, the second term on the right-hand side of the free boundary condition makes sense for $\phi_a \in H^1(\mathcal{A})$ because $\mathbf{grad}_a\,\mathbf{d}_a\mathbf{d}_a$ is also a tangential vector to Γ_a^f.

Consequently, to enforce that $\mathrm{grad}_a\,\phi_a \cdot \mathbf{d}_a$ belongs to $H^1(\mathcal{A})$, a new unknown β is introduced in model (17), which is defined by $\beta = \mathrm{grad}_a\,\phi_a \cdot \mathbf{d}_a$. Thus, problem (17) is written including the scalar field β as follows:

$$\begin{cases} \Delta_a \phi_a = 0 & \text{in } \mathcal{A}, \\ \beta = \mathrm{grad}_a\,\phi_a \cdot \mathbf{d}_a & \text{in } \mathcal{A}, \\ \dfrac{\partial \phi_a}{\partial \mathbf{n}_a} = -\dfrac{1}{g}\,\mathrm{grad}_a\,\beta \cdot \mathbf{d}_a + \dfrac{1}{g}\,\mathrm{grad}_a\,\phi_a \cdot \mathbf{grad}_a\,\mathbf{d}_a\mathbf{d}_a & \text{on } \Gamma_a^f, \\ \dfrac{\partial \phi_a}{\partial \mathbf{n}_a} = -\mathbf{v}^{ap} \cdot \mathbf{n}_a & \text{on } \Gamma_a^r, \\ \dfrac{\partial \phi_a}{\partial \mathbf{n}_a} = -\mathbf{v}_a^s \cdot \mathbf{n}_a & \text{on } \Gamma_a^b, \\ \mathrm{grad}_a\,\phi_a = \mathbf{0} & \text{for } |z - o_a| \to \infty. \end{cases} \tag{19}$$

6. Numerical resolution

In this section the numerical resolution of the steady problem (19) is discussed. With this purpose, the transport term $\mathrm{grad}_a\,\phi_a \cdot \mathbf{d}_a$ should be discretized adequately and the unbounded domain $\mathcal{A}$ truncated taking into account the radiation condition. On the one hand, since problem (19) is discretized by using a standard finite element procedure, the transport term must be conveniently treated by applying an upwinding methodology. On the other hand, a Perfectly Matched Layer technique is introduced to handle the radiation condition and to truncate the otherwise unbounded domain $\mathcal{A}$.

In order to discretize the transport term properly, the second equation of (19) will be rewritten. The proposed upwinding strategy is described in Section 6.1. This strategy is inspired by the Streamline Upwind Petrov–Galerkin (SUPG) method. In fact, it has been derived because the straightforward application of the standard SUPG method produces spurious numerical oscillations when it is combined with the PML technique. Once the bounded computational domain is described after introducing the PML layer in the original problem (19), the weak form associated with the resulting system will be written.

6.1. Upwind methodology for handling the transport term

The SUPG method (see Brooks and Hughes [14]) can be understood as a replacement of continuous weighting functions with discontinuous ones in the discretization of a Petrov–Galerkin formulation. Instead of working at the discrete finite element level, firstly an equivalent upwinded continuous problem is introduced and then a standard Galerkin method is directly applied.

With the aim of describing the upwinding strategy, the second equation of problem (19) is stated in an arbitrary domain $\mathcal{D}$,

$$\beta = \mathrm{grad}_a\,\phi_a \cdot \mathbf{d}_a \text{ in } \mathcal{D}.$$

Now, assume for a moment that φ_a is given in $H^1(\mathcal{D})$. The standard weak formulation of this equation is

$$\begin{cases} \text{Find } \beta \in L^2(\mathcal{D}) \text{ such that} \\ \displaystyle\int_{\mathcal{D}} \beta\xi\,\mathrm{dV}_z = \int_{\mathcal{D}} \mathrm{grad}_a\,\phi_a \cdot \mathbf{d}_a\xi\,\mathrm{dV}_z, \quad \forall \xi \in L^2(\mathcal{D}). \end{cases} \tag{20}$$

The modification of the test functions corresponding to the standard SUPG strategy consists in replacing the test function ξ in the weak formulation above by

$$\xi^{SUPG} := \xi + k\,\mathrm{grad}_a\,\xi\cdot\mathbf{d}_a, \tag{21}$$

where k is a function which depends on the mesh size and the magnitude of the underlying velocity $\mathbf{d}_a$ (see Brooks and Hughes [14]). To ensure that $\xi^{SUPG}\in L^2(\mathcal{D})$, it is necessary to impose $\xi\in H^1(\mathcal{D})$. In fact, since the boundary conditions do not play any relevant role in this general description, it is assumed $\xi\in H^1_0(\mathcal{D})$ for the sake of simplicity. Thus, replacing ξ by ξ^{SUPG}, the above weak formulation becomes,

$$\begin{cases}\text{Find } \beta\in L^2(\mathcal{D}) \text{ such that}\\ \displaystyle\int_{\mathcal{D}}\beta\xi\,\mathrm{dV}_z+\int_{\mathcal{D}}k\beta\,\mathrm{grad}_a\,\xi\cdot\mathbf{d}_a\mathrm{dV}_z=\int_{\mathcal{D}}\mathrm{grad}_a\,\phi_a\cdot\mathbf{d}_a\xi\,\mathrm{dV}_z+\int_{\mathcal{D}}k\,\mathrm{grad}_a\,\phi_a\cdot\mathbf{d}_a\,\mathrm{grad}_a\,\xi\cdot\mathbf{d}_a\mathrm{dV}_z,\quad\forall\xi\in H^1_0(\mathcal{D}).\end{cases} \tag{22}$$

The last step to get the final formulation consists in looking for a solution $\beta\in H^1(\mathcal{D})$. The use of a classical Green's formula in (22) leads to

$$\begin{cases}\text{Find } \beta\in H^1(\mathcal{D}) \text{ such that}\\ \displaystyle\int_{\mathcal{D}}\beta\xi\,\mathrm{dV}_z-\int_{\mathcal{D}}\mathrm{div}_a\,(k\beta\mathbf{d}_a)\xi\,\mathrm{dV}_z=\int_{\mathcal{D}}\mathrm{grad}_a\,\phi_a\cdot\mathbf{d}_a\xi\,\mathrm{dV}_z-\int_{\mathcal{D}}\mathrm{div}_a\,(k\,\mathrm{grad}_a\,\phi_a\cdot\mathbf{d}_a\mathbf{d}_a)\xi\,\mathrm{dV}_z,\quad\forall\xi\in H^1_0(\mathcal{D}).\end{cases}$$

This is a standard Galerkin weak formulation leading to the strong equation

$$\beta-\mathrm{div}_a\,(k\beta\mathbf{d}_a)=\mathrm{grad}_a\,\phi_a\cdot\mathbf{d}_a-\mathrm{div}_a\,(k\,\mathrm{grad}_a\,\phi_a\cdot\mathbf{d}_a\mathbf{d}_a)\ \text{ in }\mathcal{D}.$$

The partial differential equation written above has been deduced from the weak formulation of the classical SUPG approach (20). Only some additional regularity conditions on the involved unknown fields ϕ_a and β have been assumed. Finally, since $\mathbf{d}_a$ is divergence-free ($\mathbf{d}_a$ is the underlying velocity field of an incompressible fluid), then

$$\beta-\mathbf{d}_a\cdot\mathrm{grad}_a(k\beta)=\mathrm{grad}_a\,\phi_a\cdot\mathbf{d}_a-\mathbf{d}_a\cdot\mathrm{grad}_a(k\,\mathrm{grad}_a\,\phi_a\cdot\mathbf{d}_a)\ \text{ in }\mathcal{D}. \tag{23}$$

This strategy was also used in the numerical resolution of the classical model introduced in Remark 5.1.

In order to subsequently achieve an upwinding finite element discretization, the second equation in (19) is replaced by (23) with $k:=h_d\delta_{\mathrm{SUPG}}\frac{1}{|\mathbf{d}_a|}$, where $0\le\delta_{SUPG}\le 1$ is a constant to be chosen (throughout the entire work $\delta_{\mathrm{SUPG}}=\frac{1}{\sqrt{2}}$ as proposed in Giuliani et al. [8] for a similar problem), and h_d is the cell diameter of the finite element mesh.

Summarizing, the modified steady-state problem to be solved is the following:

$$\begin{cases}\Delta_a\phi_a=0 & \text{in }\mathcal{A},\\ \beta-\mathbf{d}_a\cdot\mathrm{grad}_a(k\beta)=\mathrm{grad}_a\,\phi_a\cdot\mathbf{d}_a-\mathbf{d}_a\cdot\mathrm{grad}_a\,(k\,\mathrm{grad}_a\,\phi_a\cdot\mathbf{d}_a) & \text{in }\mathcal{A},\\ \dfrac{\partial\phi_a}{\partial\mathbf{n}_a}=-\dfrac{1}{g}\,\mathrm{grad}_a\,\beta\cdot\mathbf{d}_a+\dfrac{1}{g}\,\mathrm{grad}_a\,\phi_a\cdot\mathbf{grad}_a\,\mathbf{d}_a\mathbf{d}_a & \text{on }\Gamma^f_a,\\ \dfrac{\partial\phi_a}{\partial\mathbf{n}_a}=-\mathbf{v}^{ap}\cdot\mathbf{n}_a & \text{on }\Gamma^r_a,\\ \dfrac{\partial\phi_a}{\partial\mathbf{n}_a}=-\mathbf{v}^{s}_a\cdot\mathbf{n}_a & \text{on }\Gamma^b_a,\\ \mathrm{grad}_a\,\phi_a=\mathbf{0} & \text{for } |z-o_a|\to\infty.\end{cases} \tag{24}$$

At this point, it should be emphasized that this methodology provides a general approach for upwinding discretizations of convective terms, which are suitable to combine with the use of PML methods to truncate the original unbounded domain.

6.2. Perfectly matched layer technique

Before discretizing problem (24), the unbounded domain $\mathcal{A}$ must be truncated and the radiation condition (see the last equation of problem (24)) must be taken into account. Both tasks are being addressed with the use of an adequate PML layer (see Appendix B for a detailed discussion). Since the fluid domain is only assumed unbounded in the horizontal spatial coordinates, the computational domain will be truncated using a cylindrical surface. Thus, the bounded computational domain consists of two subdomains: the truncated fluid domain $\mathcal{A}_F$ (where the fluid around the floating body is located), and an exterior cylindrical annulus $\mathcal{A}_\infty$ (where the PML equations hold). This truncation process is determined by two parameters: the inner and outer radius of the annulus, i.e., the radius of the fluid domain R and the outer radius of the cylindrical annulus R_∞. Hence, the two computational subdomains are given by

$$\mathcal{A}_F=\{z=(z_1,z_2,z_3)\in\mathcal{A}:z_1^2+z_2^2<R^2\},$$
$$\mathcal{A}_\infty=\{z=(z_1,z_2,z_3)\in\mathcal{A}:R^2<z_1^2+z_2^2<R_\infty^2\}.$$

The coupling boundary between both subdomains is given by $\partial\mathcal{A}^i=\partial\mathcal{A}_F\cap\partial\mathcal{A}_\infty$. Additionally, the disjoint splitting of the boundaries in $\mathcal{A}$ is also kept in the fluid and PML subdomains. Consequently, a new set of boundaries are introduced:

(a) the boundaries associated with the fluid subdomain are the free surface, $\partial\mathcal{A}^f$, the seabed, $\partial\mathcal{A}^b$, and the wet surface of the floating body, $\partial\mathcal{A}^r$, which are given by

$$\partial\mathcal{A}^f = \{z = (z_1, z_2, z_3) \in \partial\mathcal{A}_F : z_3 = 0\},$$
$$\partial\mathcal{A}^b = \partial\mathcal{A}_F \cap \Gamma_a^b,$$
$$\partial\mathcal{A}^r = \Gamma_a^r,$$

(b) the boundaries corresponding to the PML are the free surface, $\partial\mathcal{A}_\infty^f$, the seabed, $\partial\mathcal{A}_\infty^b$ and the outer vertical boundary, $\partial\mathcal{A}^\infty$. They are defined by

$$\partial\mathcal{A}_\infty^f = \{z = (z_1, z_2, z_3) \in \partial\mathcal{A}_\infty : z_3 = 0\},$$
$$\partial\mathcal{A}_\infty^b = \partial\mathcal{A}_\infty \cap \Gamma_a^b,$$
$$\partial\mathcal{A}^\infty = \{z = (z_1, z_2, z_3) \in \partial\mathcal{A}_\infty : z_1^2 + z_2^2 = R_\infty^2\}.$$

Remark 6.1. The fluid domain $\mathcal{A}$ is originally assumed to have a finite depth and hence no truncation procedures needs to be applied in the vertical spatial direction. Otherwise, if an infinite depth is considered, then the velocity potential in problem (24) would exhibit an exponential decay behaviour with respect to the coordinate z_3 and a PML layer of Laplacian type (see Trenev [20]) should be used to truncate the unbounded domain in the z_3-axis. Anyway, in both cases (with finite or infinite depth), the PML technique stated on the cylindrical annulus $\mathcal{A}_\infty$ is required due to the presence of the convective term in the free surface condition (see the third equation in problem (24)). □

The PML technique introduced in problem (24) produces an adequate absorption of waves associated with the Kelvin wake in the radial direction. Since problem (24) is a steady-state model involving the Laplace's equation, a straightforward approach could consider the use of a Laplacian-like PML (see Trenev [20] for more details). However, that PML model cannot handle the transport effects arising from the convective term on the free surface condition. Consequently, even though the presence of the floating body generates a stationary wave (the so-called Kelvin wake pattern) a wave-like PML (typical for time-harmonic problems) has been considered; more precisely, the PML model analysed by Cohen and Imperiale [13] in a two-dimensional Cartesian setting for a hydrodynamic problem with constant underlying velocity has been extended for the proposed model (24) within a three-dimensional domain written in cylindrical coordinates.

Remark 6.2. Since a time-harmonic PML model has been considered, a specific value for the angular frequency should be associated with the steady-state model (24). For this purpose, the Kelvin wake pattern can be approximated locally by a linear combination of plane waves propagating in a predominant direction which forms an angle θ_p with respect to the underlying velocity (see Newman [1] for a detailed discussion). Since the wave motion associated with the Kelvin wake is stationary (with respect to a reference framework fixed at the floating body), these local plane waves of the form $e^{-i\omega t}e^{i\boldsymbol{\kappa}\cdot(z-o_a)}$ should be time-independent, i.e., assuming that $z = p + \mathbf{v}^{ap}t$, then

$$\omega t - \boldsymbol{\kappa}\cdot(z - o_a) = (\omega - \boldsymbol{\kappa}\cdot\mathbf{v}^{ap})t + p$$

should be independent of time, or equivalently, it holds $\omega = |\boldsymbol{\kappa}|\,|\mathbf{v}^{ap}|\cos\theta_p$, where $\boldsymbol{\kappa}$ denotes the wavenumber vector. Additionally, the dispersion relation for a plane wave propagated in a fluid domain of finite depth d and a free surface is given by $\omega^2 = g|\boldsymbol{\kappa}|\tanh(|\boldsymbol{\kappa}|d)$. Hence,

$$\omega_p = \frac{g}{|\mathbf{v}^{ap}|\cos\theta_p}\tanh\left(\frac{\omega_p}{|\mathbf{v}^{ap}|\cos\theta_p}d\right), \tag{25}$$

where the value of θ_p can be approximated by $\theta_p = 0.6155$ rad (see Newman [1] for a detailed derivation). Obviously, the angular frequency ω_p is a parameter determined by the apparent velocity and the angle θ_p, which is computed ad hoc to settle the PML coefficients (see Appendix B.1 for a sensitivity analysis of the PML performance with respect to the angle θ_p). □

To derive the time-harmonic governing equations of a PML model acting as an absorber layer in the radial direction, firstly the linear problem (24) must be written in cylindrical coordinates (r, θ, z) associated with the Cartesian coordinates $z = (z_1, z_2, z_3)$ in the AL configuration. Then, taking into account that the time-harmonic PML models can be understood as a complex-stretching of the spatial coordinates (see Chew and Weedon [21]), the radial coordinate r is formally replaced by a new complex-valued function $\hat{r}$, which introduces an artificial dissipation to damp the outgoing waves. The choice of function $\hat{r}$ depends on the so-called absorption PML profile $\sigma_r : [R, R_\infty] \to \mathbb{R}^+$, which is an increasing non-negative continuous function. For the sake of simplicity, it is assumed $\sigma_r(R) = 0$. In order to write the governing equations in the PML domain, some complex-valued expressions are introduced:

$$\hat{r}(r) := r + \frac{i}{\omega_p}\int_R^r \sigma_r(s)\,\mathrm{d}s, \quad \sigma_\theta(r) := \frac{1}{r}\int_R^r \sigma_r(s)\,\mathrm{d}s, \quad \gamma(r) := \frac{\partial\hat{r}}{\partial r}(r) = 1 + \frac{i}{\omega_p}\sigma_r(r), \quad \hat{\gamma}(r) := \frac{\hat{r}}{r}(r) = 1 + \frac{i}{\omega_p}\sigma_\theta(r).$$

If r is formally replaced by $\hat{r}$, and denoting the new gradient and divergence operators with $\widehat{\ }$, then the expressions of operators grad_a, $\mathbf{grad}_a$ and div_a in cylindrical coordinates are replaced by

$$\widehat{\mathrm{grad}}_a\phi = \frac{\partial\phi}{\partial\hat{r}}\mathbf{e}_r + \frac{1}{\hat{r}}\frac{\partial\phi}{\partial\theta}\mathbf{e}_\theta + \frac{\partial\phi}{\partial z}\mathbf{e}_z,$$

$$\widehat{\mathbf{grad}}_a\mathbf{w} = \frac{\partial w_r}{\partial \hat{r}}\mathbf{e}_r\otimes\mathbf{e}_r + \left[\frac{1}{\hat{r}}\frac{\partial w_r}{\partial\theta} - \frac{1}{\hat{r}}w_\theta\right]\mathbf{e}_r\otimes\mathbf{e}_\theta + \frac{\partial w_r}{\partial z}\mathbf{e}_r\otimes\mathbf{e}_z + \frac{\partial w_\theta}{\partial\hat{r}}\mathbf{e}_\theta\otimes\mathbf{e}_r + \left[\frac{1}{\hat{r}}\frac{\partial w_\theta}{\partial\theta} + \frac{1}{\hat{r}}w_{\hat{r}}\right]\mathbf{e}_\theta\otimes\mathbf{e}_\theta + \frac{\partial w_\theta}{\partial z}\mathbf{e}_\theta\otimes\mathbf{e}_z$$
$$+ \frac{\partial w_z}{\partial\hat{r}}\mathbf{e}_z\otimes\mathbf{e}_r + \frac{1}{\hat{r}}\frac{\partial w_z}{\partial\theta}\mathbf{e}_z\otimes\mathbf{e}_\theta + \frac{\partial w_z}{\partial z}\mathbf{e}_z\otimes\mathbf{e}_z,$$
$$\widehat{\mathrm{div}}_a\mathbf{w} = \frac{1}{\hat{r}}\frac{\partial}{\partial\hat{r}}(\hat{r}w_r) + \frac{1}{\hat{r}}\frac{\partial w_\theta}{\partial\theta} + \frac{\partial w_z}{\partial z},$$

where $\{\mathbf{e}_r,\mathbf{e}_\theta,\mathbf{e}_z\}$ is the orthonormal basis associated to this coordinate system. Now, if $\hat{r}$ is replaced by $r\hat{\gamma}(r)$ and, for simplicity in notation, the tensor $\mathbf{C} := \frac{1}{\gamma}\mathbf{e}_r\otimes\mathbf{e}_r + \frac{1}{\hat{\gamma}}\mathbf{e}_\theta\otimes\mathbf{e}_\theta + \mathbf{e}_z\otimes\mathbf{e}_z$ is introduced, the PML differential operators can be rewritten as follows:

$$\widehat{\mathrm{grad}}_a\phi = \frac{1}{\gamma}\frac{\partial\phi}{\partial r}\mathbf{e}_r + \frac{1}{\hat{\gamma}r}\frac{\partial\phi}{\partial\theta}\mathbf{e}_\theta + \frac{\partial\phi}{\partial z}\mathbf{e}_z = \mathbf{C}\,\mathrm{grad}_a\,\phi,$$
$$\widehat{\mathbf{grad}}_a\mathbf{w}\mathbf{w} = \mathbf{grad}_a\,\mathbf{w}(\mathbf{C}\mathbf{w}),$$
$$\widehat{\mathrm{div}}_a\mathbf{w} = \frac{1}{\hat{\gamma}\gamma r}\frac{\partial}{\partial r}(r\hat{\gamma}w_r) + \frac{1}{\hat{\gamma}r}\frac{\partial w_\theta}{\partial\theta} + \frac{\partial w_z}{\partial z} = \frac{1}{\hat{\gamma}\gamma}\left(\frac{1}{r}\frac{\partial}{\partial r}(r\hat{\gamma}w_r) + \frac{1}{r}\frac{\partial w_\theta}{\partial\theta}(\gamma w_\theta) + \frac{\partial}{\partial z}(\gamma\hat{\gamma}w_z)\right) = \det(\mathbf{C})\,\mathrm{div}_a(\det(\mathbf{C})^{-1}\mathbf{C}\mathbf{w}).$$

Notice that $\mathbf{C}$ is diagonal in the cylindrical reference system. Therefore,

$$\hat{\Delta}_a\hat{\phi}_a = \widehat{\mathrm{div}}_a(\widehat{\mathrm{grad}}_a\hat{\phi}_a) = \det(\mathbf{C})\,\mathrm{div}_a(\det(\mathbf{C})^{-1}\mathbf{C}\mathbf{C}\,\mathrm{grad}_a\,\hat{\phi}_a) = \frac{1}{\hat{\gamma}\gamma}\left(\frac{1}{r}\frac{\partial}{\partial r}\left(\frac{\hat{\gamma}}{\gamma}r\frac{\partial\hat{\phi}_a}{\partial r}\right) + \frac{\gamma}{\hat{\gamma}}\frac{1}{r^2}\frac{\partial^2\hat{\phi}_a}{\partial\theta^2} + \gamma\hat{\gamma}\frac{\partial^2\hat{\phi}_a}{\partial z^2}\right).$$

By an analogous procedure, the equation associated with the transport term can be obtained, namely,

$$\hat{\beta} - \mathbf{d}_a\cdot\widehat{\mathrm{grad}}_a(k\hat{\beta}) = \widehat{\mathrm{grad}}_a\hat{\phi}_a\cdot\mathbf{d}_a - \mathbf{d}_a\cdot\widehat{\mathrm{grad}}_a\left(k\widehat{\mathrm{grad}}_a\hat{\phi}_a\cdot\mathbf{d}_a\right)\ \text{in}\ \mathcal{A}_\infty,$$

or, equivalently,

$$\hat{\beta} - \mathbf{d}_a\cdot\mathbf{C}\,\mathrm{grad}_a(k\hat{\beta}) = \mathbf{C}\,\mathrm{grad}_a\,\hat{\phi}_a\cdot\mathbf{d}_a - \mathbf{d}_a\cdot\mathbf{C}\,\mathrm{grad}_a\left(k\mathbf{C}\,\mathrm{grad}_a\,\hat{\phi}_a\cdot\mathbf{d}_a\right)\ \text{in}\ \mathcal{A}_\infty, \tag{26}$$

which is a similar equation to the second equation in (24).

As the last step, the boundary conditions on the free surface of the PML have to be derived. Firstly, an analogous equation to the third equation in (24) can be written, as follows:

$$\widehat{\mathrm{grad}}_a\hat{\phi}_a\cdot\mathbf{n}_\infty = -\frac{1}{g}\widehat{\mathrm{grad}}_a\,\hat{\beta}\cdot\mathbf{d}_a + \frac{1}{g}\widehat{\mathrm{grad}}_a\hat{\phi}_a\cdot\widehat{\mathbf{grad}}_a\mathbf{d}_a\mathbf{d}_a\ \text{on}\ \partial\mathcal{A}^f_\infty,$$

which is equivalent to

$$\mathbf{C}\,\mathrm{grad}_a\,\hat{\phi}_a\cdot\mathbf{n}_\infty = -\frac{1}{g}\mathbf{C}\,\mathrm{grad}_a\,\hat{\beta}\cdot\mathbf{d}_a + \frac{1}{g}\mathbf{C}\,\mathrm{grad}_a\,\hat{\phi}_a\cdot\mathbf{grad}_a\,\mathbf{d}_a(\mathbf{C}\mathbf{d}_a)\ \text{on}\ \partial\mathcal{A}^f_\infty.$$

Since $\mathbf{n}_\infty = \mathbf{g}_3$ on $\partial\mathcal{A}^f_\infty$ then $\mathbf{n}_\infty = \mathbf{C}\mathbf{n}_\infty$, and so the above equation is also equivalent to

$$\det(\mathbf{C}^{-1})\mathbf{C}\mathbf{C}\,\mathrm{grad}_a\,\hat{\phi}_a\cdot\mathbf{n}_\infty = -\frac{1}{g}\det(\mathbf{C}^{-1})\mathbf{C}\,\mathrm{grad}_a\,\hat{\beta}\cdot\mathbf{d}_a + \frac{1}{g}\det(\mathbf{C}^{-1})\mathbf{C}\,\mathrm{grad}_a\,\hat{\phi}_a\cdot\mathbf{grad}_a\,\mathbf{d}_a(\mathbf{C}\mathbf{d}_a)\ \text{on}\ \partial\mathcal{A}^f_\infty.$$

Similarly, the boundary condition on the seabed in the PML domain takes the form

$$\det(\mathbf{C}^{-1})\mathbf{C}\mathbf{C}\,\mathrm{grad}_a\,\hat{\phi}_a\cdot\mathbf{n}_\infty = -\det(\mathbf{C}^{-1})\mathbf{v}^s_a\cdot\mathbf{n}_\infty\ \text{on}\ \partial\mathcal{A}^b_\infty.$$

Finally, for the sake of simplicity the notation $\mathbf{S} := \det(\mathbf{C}^{-1})\mathbf{C}\mathbf{C}$ is introduced. Since $\det(\mathbf{C})\neq 0$ then the system of governing equations in the PML subdomain is

$$\begin{cases}
\mathrm{div}_a\left(\mathbf{S}\,\mathrm{grad}_a\,\hat{\phi}_a\right) = 0 & \text{in}\ \mathcal{A}_\infty,\\
\hat{\beta} - \mathbf{d}_a\cdot\mathbf{C}\,\mathrm{grad}_a(k\hat{\beta}) = \mathbf{C}\,\mathrm{grad}_a\,\hat{\phi}_a\cdot\mathbf{d}_a - \mathbf{d}_a\cdot\mathbf{C}\,\mathrm{grad}_a\left(k\mathbf{C}\,\mathrm{grad}_a\,\hat{\phi}_a\cdot\mathbf{d}_a\right) & \text{in}\ \mathcal{A}_\infty,\\
\mathbf{S}\,\mathrm{grad}_a\,\hat{\phi}_a\cdot\mathbf{n}_\infty = -\frac{1}{g}\det(\mathbf{C}^{-1})\mathbf{C}\,\mathrm{grad}_a\,\hat{\beta}\cdot\mathbf{d}_a + \frac{1}{g}\det(\mathbf{C}^{-1})\mathbf{C}\,\mathrm{grad}_a\,\hat{\phi}_a\cdot\mathbf{grad}_a\,\mathbf{d}_a(\mathbf{C}\mathbf{d}_a) & \text{on}\ \partial\mathcal{A}^f_\infty,\\
\mathbf{S}\,\mathrm{grad}_a\,\hat{\phi}_a\cdot\mathbf{n}_\infty = -\det(\mathbf{C}^{-1})\mathbf{v}^s_a\cdot\mathbf{n}_\infty & \text{on}\ \partial\mathcal{A}^b_\infty,\\
\hat{\phi}_a = 0 & \text{on}\ \partial\mathcal{A}^\infty,\\
\hat{\beta} = 0 & \text{on}\ \partial\mathcal{A}^\infty,
\end{cases} \tag{27}$$

and in the fluid subdomain,

$$\begin{cases} \Delta_a \phi_a = 0 & \text{in } \mathcal{A}_F, \\ \beta - \mathbf{d}_a \cdot \operatorname{grad}_a(k\beta) = \operatorname{grad}_a \phi_a \cdot \mathbf{d}_a - \mathbf{d}_a \cdot \operatorname{grad}_a (k \operatorname{grad}_a \phi_a \cdot \mathbf{d}_a) & \text{in } \mathcal{A}_F, \\ \dfrac{\partial \phi_a}{\partial \mathbf{n}_a} = -\dfrac{1}{g} \operatorname{grad}_a \beta \cdot \mathbf{d}_a + \dfrac{1}{g} \operatorname{grad}_a \phi_a \cdot \mathbf{grad}_a \mathbf{d}_a \mathbf{d}_a & \text{on } \partial\mathcal{A}^f, \\ \dfrac{\partial \phi_a}{\partial \mathbf{n}_a} = -\mathbf{v}^{ap} \cdot \mathbf{n}_a & \text{on } \partial\mathcal{A}^r, \\ \dfrac{\partial \phi_a}{\partial \mathbf{n}_a} = -\mathbf{v}_a^s \cdot \mathbf{n}_a & \text{on } \partial\mathcal{A}^b. \end{cases} \tag{28}$$

The unknown fields in the fluid and the PML subdomains are coupled by the transmission conditions

$$\begin{aligned} &\phi_a = \hat{\phi}_a && \text{on } \partial\mathcal{A}^i, \\ &\frac{\partial \phi_a}{\partial \mathbf{n}_a} = -\mathbf{S} \operatorname{grad}_a \hat{\phi}_a \cdot \mathbf{n}_\infty && \text{on } \partial\mathcal{A}^i, \\ &\beta = \hat{\beta} && \text{on } \partial\mathcal{A}^i, \end{aligned} \tag{29}$$

where $\mathbf{n}_\infty = -\mathbf{n}_a$ on $\partial\mathcal{A}^i$.

6.3. Weak formulation

Once the convective terms have been handled with an adequate upwinding strategy and the use of a cylindrical PML layer ensures an accurate damping of the outgoing waves in the truncated computational domain, the governing equations in the fluid and the PML subdomains must be written in a weak form. With this aim, a convenient function space W must be introduced, where the unknown field pairs $(\phi_a, \hat{\phi}_a)$ and $(\beta, \hat{\beta})$ are sought. So, the functional space W is defined by

$$W := \left\{ (u, \hat{u}) \in H^1(\mathcal{A}_F) \times H^1(\mathcal{A}_\infty) : u|_{\partial\mathcal{A}^i} = \hat{u}\big|_{\partial\mathcal{A}^i},\ \hat{u}\big|_{\partial\mathcal{A}^\infty} = 0 \right\}.$$

In order to obtain a weak formulation of the strong problem (27)–(29), test functions $(\psi, \hat{\psi}),\ (\xi, \hat{\xi}) \in W$ are considered. Before writing the weak formulation, it is necessary to define $\mathcal{A}_U$ as the interior set of the closure of the union of the fluid subdomain with the PML subdomain, $\mathcal{A}_U := \operatorname{Int}\big(\overline{\mathcal{A}_F \cup \mathcal{A}_\infty}\big)$, to introduce the spaces corresponding to $\mathbf{d}_a \in (H^1(\mathcal{A}_U))^3$, and $k \in L^\infty(\mathcal{A}_U)$. Then, by applying standard procedures involving Green's formulas and using the boundary conditions of problem (8) (assuming $\Gamma_a^f = \partial\mathcal{A}^f \cup \partial\mathcal{A}_\infty^f$, $\Gamma_a^b = \partial\mathcal{A}^b \cup \partial\mathcal{A}_\infty^b$ and $\Gamma_a^r = \partial\mathcal{A}^r$) and some properties of tensor $\mathbf{C}$ (namely, its symmetry, $\mathbf{C}|_{\partial\mathcal{A}^i} = \mathbf{I}$ and $\mathbf{C}\mathbf{n}_\infty = \mathbf{n}_\infty$ on $\partial\mathcal{A}_\infty^f \cup \partial\mathcal{A}_\infty^b$), it is straightforward to get the following weak formulation:

$$\begin{cases} \text{Given } \mathbf{d}_a \in (H^1(\mathcal{A}_U))^3 \text{ and } k \in L^\infty(\mathcal{A}_U),\ \text{find } (\phi_a, \hat{\phi}_a), (\beta, \hat{\beta}) \in W \text{ such that} \\ \displaystyle\int_{\mathcal{A}_F} \operatorname{grad}_a \phi_a \cdot \operatorname{grad}_a \psi \, \mathrm{dV}_z + \frac{1}{g} \int_{\partial\mathcal{A}^f} \operatorname{grad}_a \beta \cdot \mathbf{d}_a \psi \, \mathrm{dA}_z - \frac{1}{g} \int_{\partial\mathcal{A}^f} \operatorname{grad}_a \phi_a \cdot \mathbf{grad}_a \mathbf{d}_a \mathbf{d}_a \psi \, \mathrm{dA}_z \\ \displaystyle + \int_{\mathcal{A}_\infty} \mathbf{S} \operatorname{grad}_a \hat{\phi}_a \cdot \operatorname{grad}_a \hat{\psi} \, \mathrm{dV}_z + \frac{1}{g} \int_{\partial\mathcal{A}_\infty^f} \det(\mathbf{C}^{-1}) \mathbf{C} \operatorname{grad}_a \hat{\beta} \cdot \mathbf{d}_a \hat{\psi} \, \mathrm{dA}_z \\ \displaystyle - \frac{1}{g} \int_{\partial\mathcal{A}_\infty^f} \det(\mathbf{C}^{-1}) \mathbf{C} \operatorname{grad}_a \hat{\phi}_a \cdot \mathbf{grad}_a \mathbf{d}_a (\mathbf{C}\mathbf{d}_a) \hat{\psi} \, \mathrm{dA}_z = - \int_{\partial\mathcal{A}^r} \mathbf{v}^{ap} \cdot \mathbf{n}_a \psi \, \mathrm{dA}_z - \int_{\partial\mathcal{A}^b} \mathbf{v}_a^s \cdot \mathbf{n}_a \psi \, \mathrm{dA}_z \\ \displaystyle - \int_{\partial\mathcal{A}_\infty^b} \det(\mathbf{C}^{-1}) \mathbf{v}_a^s \cdot \mathbf{n}_\infty \hat{\psi} \, \mathrm{dA}_z \qquad \forall (\psi, \hat{\psi}) \in W, \\ \displaystyle \int_{\mathcal{A}_F} \beta \xi \, \mathrm{dV}_z + \int_{\mathcal{A}_F} k\beta \mathbf{d}_a \cdot \operatorname{grad}_a \xi \, \mathrm{dV}_z - \int_{\partial\mathcal{A}^r} k\beta \mathbf{v}_a^r \cdot \mathbf{n}_a \xi \, \mathrm{dA}_z - \int_{\mathcal{A}_F} \operatorname{grad}_a \phi_a \cdot \mathbf{d}_a \xi \, \mathrm{dV}_z \\ \displaystyle - \int_{\mathcal{A}_F} k \operatorname{grad}_a \phi_a \cdot \mathbf{d}_a \mathbf{d}_a \cdot \operatorname{grad}_a \xi \, \mathrm{dV}_z + \int_{\partial\mathcal{A}^r} k \operatorname{grad}_a \phi_a \cdot \mathbf{d}_a \mathbf{v}_a^r \cdot \mathbf{n}_a \xi \, \mathrm{dA}_z \\ \displaystyle + \int_{\mathcal{A}_\infty} \hat{\beta} \hat{\xi} \, \mathrm{dV}_z + \int_{\mathcal{A}_\infty} k\hat{\beta} \operatorname{div}_a(\mathbf{C}\mathbf{d}_a \hat{\xi}) \mathrm{dV}_z - \int_{\mathcal{A}_\infty} \mathbf{C} \operatorname{grad}_a \hat{\phi}_a \cdot \mathbf{d}_a \hat{\xi} \mathrm{dV}_z \\ \displaystyle - \int_{\mathcal{A}_\infty} k\mathbf{C} \operatorname{grad}_a \hat{\phi}_a \cdot \mathbf{d}_a \operatorname{div}_a(\mathbf{C}\mathbf{d}_a \hat{\xi}) \mathrm{dV}_z = 0 \qquad \forall (\xi, \hat{\xi}) \in W. \end{cases} \tag{30}$$

Remark 6.3. The underlying velocity $\mathbf{d}_a$ is computed from the approximation of the solution of (9), $\mathbf{d}_a = \operatorname{grad}_a \phi_0 + \mathbf{v}_a^s$, plus a projection in the vectorial Sobolev space $(H^1(\mathcal{A}_U))^3$. As mentioned in Section 3, the numerical resolution of system (9) can avoid the use of large computational domains. Then, the solution $\phi_0 \in H^1(\mathcal{A}_U)$ can be approximated without using the PML technique, with the same mesh, taking the PML subdomain as fluid domain and imposing a null Dirichlet condition on the outer vertical boundary of the PML subdomain $(\partial\mathcal{A}^\infty)$. □

6.4. Discrete space

The discretization of the weak form (30) is based on a standard finite element method associated with a compatible tetrahedral mesh $\mathcal{T}_F^h$ and $\mathcal{T}_\infty^h$ of the domains $\mathcal{A}_F$ and $\mathcal{A}_\infty$, respectively. Let $X^h(\mathcal{A}_U) \subset H^1(\mathcal{A}_U)$, be the standard discrete space

consisting of continuous piecewise kth degree polynomial functions and $W^h = \{(u,\hat{u}) \in W : u \in X^h(\mathcal{A}_F), \hat{u} \in X^h(\mathcal{A}_\infty)\} \subset W$. Let $Y^h \subset L^\infty(\mathcal{A}_U)$ be the discrete space of piecewise constant functions. Then, the discrete variational formulation is described as follows:

$$
\begin{cases}
\text{Given } \mathbf{d}_a^h \in (X^h(\mathcal{A}_U))^3 \text{ and } k^h \in Y^h, \text{ find } (\phi_a^h, \hat{\phi}_a^h), (\beta^h, \hat{\beta}^h) \in W^h \text{ such that} \\
\displaystyle\int_{\mathcal{A}_F} \mathrm{grad}_a\, \phi_a^h \cdot \mathrm{grad}_a\, \psi^h \mathrm{dV}_z + \frac{1}{g}\int_{\partial\mathcal{A}^f} \mathrm{grad}_a\, \beta^h \cdot \mathbf{d}_a^h \psi^h \mathrm{dA}_z - \frac{1}{g}\int_{\partial\mathcal{A}^f} \mathrm{grad}_a\, \phi_a^h \cdot \mathbf{grad}_a\, \mathbf{d}_a^h \mathbf{d}_a^h \psi^h \mathrm{dA}_z \\
\displaystyle+\int_{\mathcal{A}_\infty} \mathbf{S}\,\mathrm{grad}_a\, \hat{\phi}_a^h \cdot \mathrm{grad}_a\, \hat{\psi}^h \mathrm{dV}_z + \frac{1}{g}\int_{\partial\mathcal{A}_\infty^f} \det(\mathbf{C}^{-1})\mathbf{C}\,\mathrm{grad}_a\, \hat{\beta}^h \cdot \mathbf{d}_a^h \hat{\psi}^h \mathrm{dA}_z \\
\displaystyle-\frac{1}{g}\int_{\partial\mathcal{A}_\infty^f} \det(\mathbf{C}^{-1})\mathbf{C}\,\mathrm{grad}_a\, \hat{\phi}_a^h \cdot \mathbf{grad}_a\, \mathbf{d}_a^h (\mathbf{C}\mathbf{d}_a^h) \hat{\psi}^h \mathrm{dA}_z = -\int_{\partial\mathcal{A}^r} \mathbf{v}^{ap} \cdot \mathbf{n}_a \psi^h \mathrm{dA}_z - \int_{\partial\mathcal{A}^b} \mathbf{v}_a^s \cdot \mathbf{n}_a \psi^h \mathrm{dA}_z \\
\displaystyle-\int_{\partial\mathcal{A}_\infty^b} \det(\mathbf{C}^{-1})\mathbf{v}_a^s \cdot \mathbf{n}_\infty \hat{\psi}^h \mathrm{dA}_z \qquad \forall (\psi^h, \hat{\psi}^h) \in W^h, \\
\displaystyle\int_{\mathcal{A}_F} \beta^h \xi^h \mathrm{dV}_z + \int_{\mathcal{A}_F} k^h \beta^h \mathbf{d}_a^h \cdot \mathrm{grad}_a\, \xi^h \mathrm{dV}_z - \int_{\partial\mathcal{A}^r} k^h \beta^h \mathbf{v}_a^r \cdot \mathbf{n}_a \xi^h \mathrm{dA}_z - \int_{\mathcal{A}_F} \mathrm{grad}_a\, \phi_a^h \cdot \mathbf{d}_a^h \xi^h \mathrm{dV}_z \\
\displaystyle-\int_{\mathcal{A}_F} k^h\, \mathrm{grad}_a\, \phi_a^h \cdot \mathbf{d}_a^h \mathbf{d}_a^h \cdot \mathrm{grad}_a\, \xi^h \mathrm{dV}_z + \int_{\partial\mathcal{A}^r} k^h\, \mathrm{grad}_a\, \phi_a^h \cdot \mathbf{d}_a^h \mathbf{v}_a^r \cdot \mathbf{n}_a \xi^h \mathrm{dA}_z \\
\displaystyle+\int_{\mathcal{A}_\infty} \hat{\beta}^h \hat{\xi}^h \mathrm{dV}_z + \int_{\mathcal{A}_\infty} k^h \hat{\beta}^h\, \mathrm{div}_a(\mathbf{C}\mathbf{d}_a^h \hat{\xi}^h) \mathrm{dV}_z - \int_{\mathcal{A}_\infty} \mathbf{C}\,\mathrm{grad}_a\, \hat{\phi}_a^h \cdot \mathbf{d}_a^h \hat{\xi}^h \mathrm{dV}_z \\
\displaystyle-\int_{\mathcal{A}_\infty} k^h \mathbf{C}\,\mathrm{grad}_a\, \hat{\phi}_a^h \cdot \mathbf{d}_a^h\, \mathrm{div}_a(\mathbf{C}\mathbf{d}_a^h \hat{\xi}^h) \mathrm{dV}_z = 0 \qquad \forall (\xi^h, \hat{\xi}^h) \in W^h.
\end{cases}
$$

Remark 6.4. Function k is a measure of the size of each element, hence it is a constant function per element and can be represented as a function in the discrete space Y^h. Moreover, the underlying velocity $\mathbf{d}_a = \mathrm{grad}_a\, \phi_0 + \mathbf{v}_a^s$ is computed from the approximated solution ϕ_0^h of problem (9) by means of $\mathbf{d}_a^h = \Pi_h(\mathrm{grad}_a\, \phi_0^h) + \mathbf{v}_a^s$, where Π_h is the L^2-projection into the discrete space $(X^h(\mathcal{A}_U))^3$ (see Remark 6.3). □

7. Numerical results

In this section the numerical simulation of the steady motion of the fluid produced by the movement of a floating body is described in detail. First, a brief description of the geometry is introduced and the meshes used in the numerical experiments are shown in Section 7.1. Second, a preliminary study of the accuracy of the PML is performed in Section 7.2. Third, the numerical results of the proposed linear approach are compared with those obtained with other linear model, the classical linear model (18) (presented in Newman [1] and used in Giuliani et al. [8]). Moreover, the same test problem has been modelled by a turbulent $k-\omega$ model coupled with the full Navier–Stokes equations, considering the free surface as the interface between two species: air and water (solved with a widely used commercial software: Ansys Fluent). The three kinds of numerical results have been compared with respect to available experimental data (see Kajitani et al. [17]) in Section 7.3. Finally, in Section 7.4 the effect of the finite element discretization on the accuracy of the numerical results is analysed by comparing the proposed linear model, the classical model (18), and the experimental results in a variety of scenarios: considering different underlying velocities, using different meshes and linear and quadratic finite elements. The results shown below have been obtained with a computational code written in `Python`, where the `FEniCS` library (see Alnæs et al. [22], Logg et al. [23]) has been used.

7.1. Wigley hull. Experimental data

The Wigley hull is a geometry commonly used as benchmark in hydrodynamic simulations due to the availability of experimental data from the bibliography (see, for instance, Kajitani et al. [17]). The shape of the Wigley hull has an analytic expression: a point $(x,y,z) \in \mathbb{R}^3$ belongs to the Wigley hull if and only if

$$
y = \frac{B_w}{2}\left(1-\left(\frac{2x}{L_w}\right)^2\right)\left(1-\left(\frac{z}{D_w}\right)^2\right) \quad x \in \left[-\frac{L_w}{2}, \frac{L_w}{2}\right] \text{ and } z \in [-D_w, 0], \tag{31}
$$

where B_w denotes the beam at midship, L_w the waterline length and D_w the draft at midship; throughout all the numerical simulations, $B_w = 0.25$, $L_w = 2.5$ and $D_w = 0.156$. Since this hull is symmetric with respect to the XZ-plane then its symmetry has been considered in the numerical simulation.

Taking into account the symmetry of this computational domain and assuming that the apparent and stream velocity are parallel to the longitudinal axis of the Wigley hull, the solution of the weak problem is symmetric with respect to its axis and hence only the half of the computational domain is considered, imposing an homogeneous Neumann condition on the plane of symmetry.

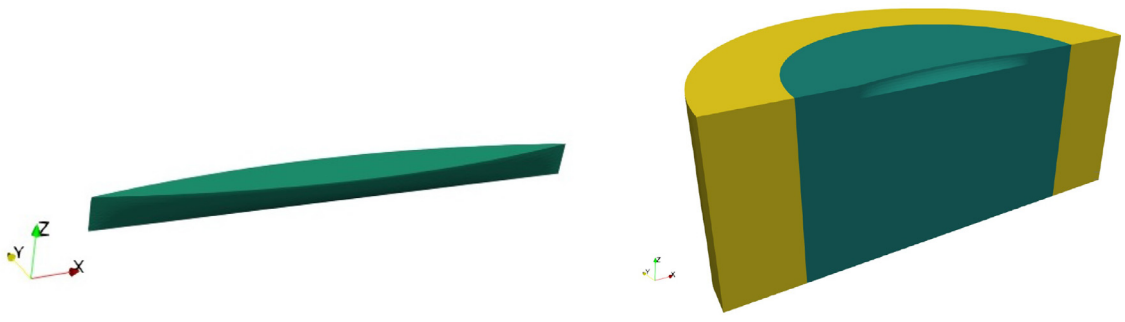

(a) Surface of the Wigley hull (b) Fluid and PML subdomains

Fig. 3. Surface of the Wigley hull on the left, with 2.5 m waterline length, 0.25 m beam at midship and 0.156 m depth at midship. Computational domain of 2.35 m of depth, on the right, consisting in a fluid subdomain with a radius of two meters (highlighted in green) and PML cylindrical annular subdomain with a thickness of one meter (highlighted in yellow). (For interpretation of the references to colour in this figure legend, the reader is referred to the web version of this article.)

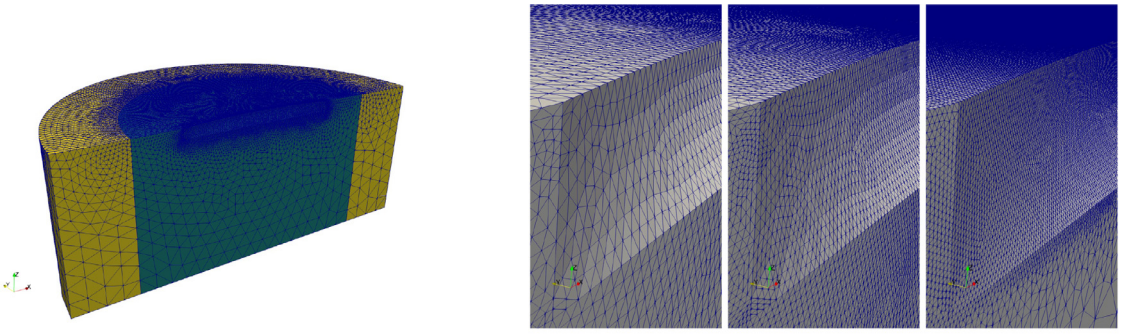

(a) Compatible fluid and PML meshes (b) From left to right: "coarse", "fine" and "very fine" mesh on the bow

Fig. 4. Computational meshes with a local refinement on the free surface and on the wet surface, where the fluid and PML subdomains are highlighted in green and yellow respectively (left). A closer detail of the mesh refinements on the bow of the Wigley hull (right). (For interpretation of the references to colour in this figure legend, the reader is referred to the web version of this article.)

The available Wigley experimental data has been obtained from Kajitani et al. [17], where the experiments involve a Wigley hull in motion aligned with its main edge at different apparent velocities. To reproduce numerically the experimental data, different Froude numbers, $\mathrm{Fr} := \frac{|\mathbf{v}^{ap}|}{\sqrt{gL_w}}$ has been considered, more precisely, $\mathrm{Fr} = 0.25, 0.267, 0.289, 0.316, 0.354, 0.408$ for those simulations where the free surface elevation is reported and $\mathrm{Fr} = 0.25, 0.267, 0.289, 0.316$ for the numerical results where the resistance coefficient is computed.

All the numerical simulations with PML shown in this work involve a fluid domain with 2 m radius ($R = 2$) and a PML with 1 m thick ($R_\infty = 3$) and 2.35 m depth (see Fig. 3, left). The dimensions of the hull and the depth correspond to the experiments reported in Kajitani et al. [17].

Three different meshes were considered in this work (see Fig. 4, where a detailed view of the meshes near of the bow of the floating body are shown on the right panels). The wet surface of the Wigley hull and the free surface have been successively refined in these three meshes (labelled as "coarse", "fine" and "very fine", respectively) in order to capture accurately the Kelvin wake pattern. The "coarse" mesh contains 362 thousands tetrahedra, the "fine" mesh is a direct refinement by splitting the tetrahedra of the "coarse" mesh with 2.8 millions tetrahedra, and the "very fine" mesh contains 3.7 millions of tetrahedra. The number of nodes on the length and height of the wet surface of the floating body, and through the wake (radial direction) for each of these meshes are reported in Table 2.

7.2. PML absorption profile

The definition of the absorption profile in the PML, $\sigma_r : [R, R_\infty) \to \mathbb{R}^+$, involves the prescription of an increasing non-negative function. In this work, a high-order polynomial approximation of the following singular absorption profile was used:

$$\sigma_r(r) = \frac{\sigma_0}{R_\infty - r} - \frac{\sigma_0}{R_\infty - R}, \tag{32}$$

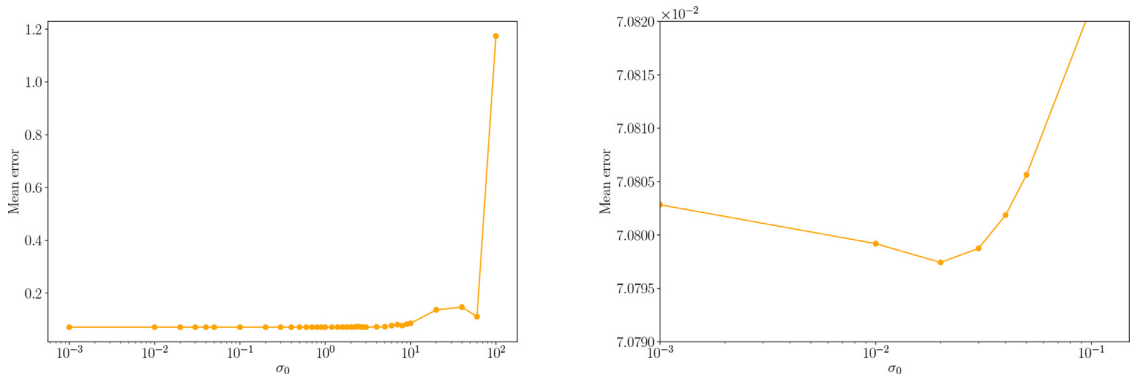

Fig. 5. Mean relative difference computed from six different numerical simulations plotted with respect to σ_0 (Right: range $\sigma_0 \in [10^{-3}, 2 \times 10^{-1}]$; left: range $\sigma_0 \in [10^{-3}, 10^2]$).

where σ_0 is a given positive parameter. In this manner, the pointwise values of the singular PML absorption profile and its polynomial approximation are identical at the quadrature nodes used in the finite element discretization. Moreover, the PML coefficients involved in the weak formulation are well defined on the entire discrete computational domain.

In order to select an optimal value for to σ_0 in the PML absorption profile, a reference solution was computed in a very large domain, which is truncated with homogeneous boundary conditions. For this purpose, a computational fluid domain with an exterior radius of 40 m has been chosen to compute the reference solution. Then, a quantitative comparison has been made to evaluate the relation between the reference result (computed in the large domain without PML), ϕ_{ref}, and the solution ϕ of the problem (19) (computed in a smaller domain truncated with a PML layer). More precisely, the L^2-relative difference between both potentials is computed on the free surface by means of

$$\frac{\|\phi_{ref} - \phi\|_2}{\|\phi_{ref}\|_2} = \frac{\left(\int_{\partial\mathcal{A}f} |\phi_{ref} - \phi|^2 \mathrm{dA}_z\right)^{\frac{1}{2}}}{\left(\int_{\partial\mathcal{A}f} |\phi_{ref}|^2 \mathrm{dA}_z\right)^{\frac{1}{2}}} \tag{33}$$

in six different numerical simulations with Froude numbers $\mathrm{Fr} = 0.25,\ 0.267,\ 0.289,\ 0.316,\ 0.354,\ 0.408$. After a swept in σ_0 from 10^{-3} to 10^2, the value $\sigma_0 = 0.02$ has been chosen since it minimizes the arithmetic mean of the L^2-relative differences computed from the six numerical approximations (see Fig. 5). The minimum error for this optimal value of σ_0 is approximately 7% whereas the relative error would reach 16.8% if the computational domain were truncated without PML (i.e., considering $\sigma_0 = 0$ on the same mesh).

Additionally, Fig. 6 shows a qualitative comparison between the reference potential and the potential obtained with the PML technique ($\sigma_0 = 0.02$) in the smallest computational domain, for the case of $\mathrm{Fr} = 0.25$ (notice that only a portion of the largest domain used for computing the reference solution is depicted). The spatial pattern of the absolute difference $|\phi_{ref} - \phi_a|$ between the reference potential and the approximated potential computed with the PML technique is also reported in the bottom panel of Fig. 6.

7.3. Numerical comparison with experimental data and full Navier–Stokes approximations

In this section, the proposed model, the classical linear potential model (18), and the full Navier–Stokes with two species are compared with the available experimental data at $\mathrm{Fr} = 0.267$. More precisely, the classical linear potential model has been already described in Remark 5.1 and a turbulence $k - \omega$ model coupled with the full Navier–Stokes equations (see Wilcox [24]) was solved in a computational domain with two species: air over the water to model the free surface boundary (using a volume of fluid method, see Hirt and Nichols [25]). Both fluids have been considered as incompressible. The use of a turbulence $k - \omega$ model makes it necessary to add boundary conditions for turbulence. For this purpose, the turbulence intensity and the turbulence length scale were set at 2.45% and 0.095 m, respectively, on inlet and outlet boundaries. Regarding the used computational domains, the classical linear model and the one proposed in the present work have been discretized using the same mesh. Analogous upwinding and PML techniques have been used in both cases. In the case of the Navier–Stokes model, a prism was chosen, no PML layers are involved and in order to deal with the displacement of the floating body the apparent constant velocity was used to include the forwarding constant velocity of the ship in the stream constant velocity. Analogous to the linear potential models, the symmetry with respect to the longitudinal plane of the Wigley hull has been used to restrict the computational domain to one half. In order to recover the interface between the two fluid phases, a refinement was imposed on the plane $z = 0$ and, thus, its discretization involves a mesh with 33 millions of tetrahedra approximately. The full two-phase Navier–Stokes model has been solved numerically using Ansys Fluent. A set of control points located on the wake support has been used to define the convergence stop criterion. Once constant values are reached at these points, the solution is assumed to be steady-state and the iterative process is stopped.

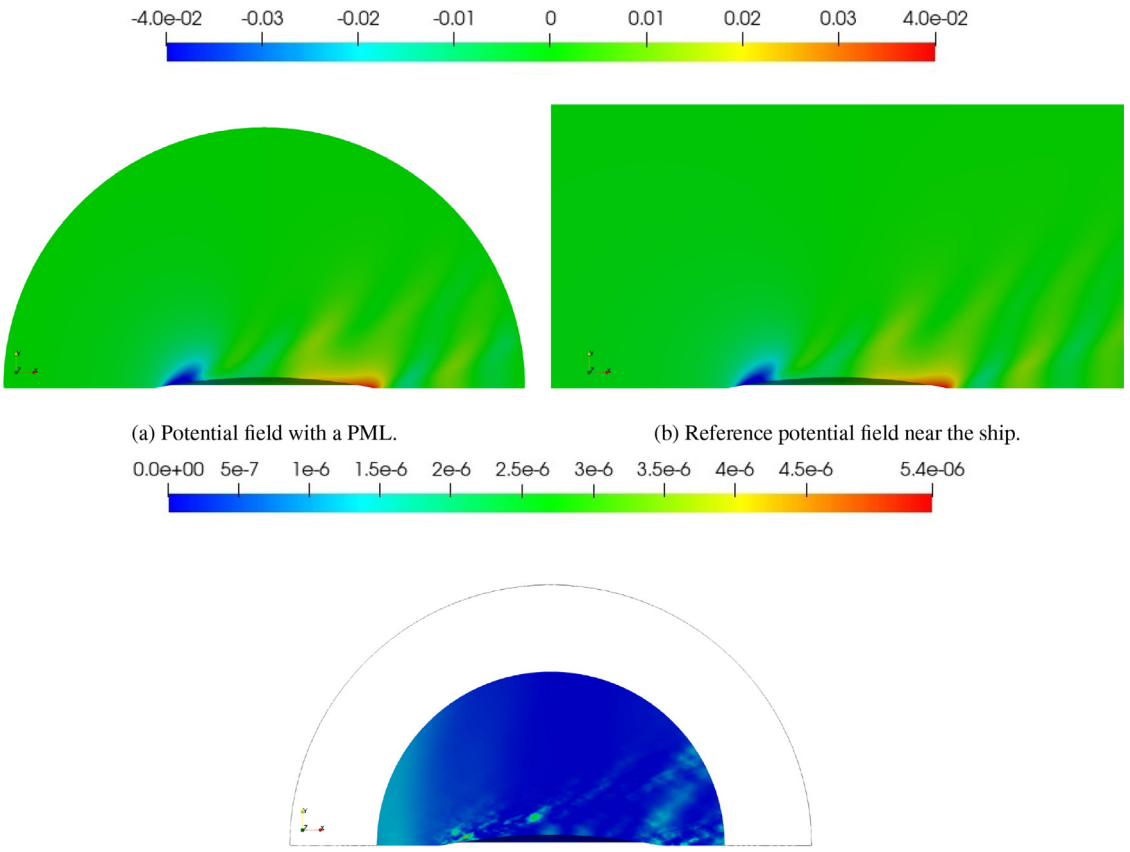

(a) Potential field with a PML.

(b) Reference potential field near the ship.

(c) Absolute difference $|\phi_{ref} - \phi_a|$ computed in the fluid domain.

Fig. 6. Left: potential field, ϕ_a, for the experiment of the Wigley hull fixed to sink and trim with Fr = 0.25, obtained using the present model with PML. Right: a zoom of the reference potential field without PML in a big domain with 40 m radius.

The maximum number of iterations has been fixed to 10000. Regarding the computational cost (CPU time), this numerical simulation needed 3 days of CPU time running on 30 threads in parallel. The computational CPU time has been measured using 4 nodes of a cluster server, where each node has 4 processors `Intel(R) Xeon(R) Gold 6126 CPU @ 2.60 GHz` and 380 GB of RAM.

Fig. 7 shows the numerical approximation of the non-dimensional free surface elevation as a function of the non-dimensional position along the Wigley hull waterline, x/L_w, for the three models as well as the experimental results, with Fr = 0.267. For the linear models, the finest mesh (shown in Fig. 4) has been used and the numerical free surface elevation was computed by

$$\eta_a = -\frac{1}{g}\,\mathrm{grad}_a\,\phi_a \cdot \mathbf{v}^{ap}, \tag{34}$$

as suggested in Giuliani et al. [8]. In all cases, for a direct comparison with the available experimental data, Kajitani et al. [17], the non-dimensional quantity $\tilde{\eta} = 2g\eta_a/|\mathbf{v}^{ap}|^2$ has been plotted.

In order to compare the flow downstream, Fig. 8 shows the three components of the velocity computed using these three different models. The full two-phase Navier–Stokes model and the proposed model show a similar pattern, except for the region of the wake aligned with the edge on the stern. However, the full two-phase Navier–Stokes model seems to damp the wake oscillations more than the proposed model as it can be observed in Fig. 7. Regarding the classical linear model (see Fig. 8), the wake angle (angle between the main Wigley axis and the line where the maxima/minima of the wake pattern are located) and the amplitude of the velocity potential are smaller than in the other two models.

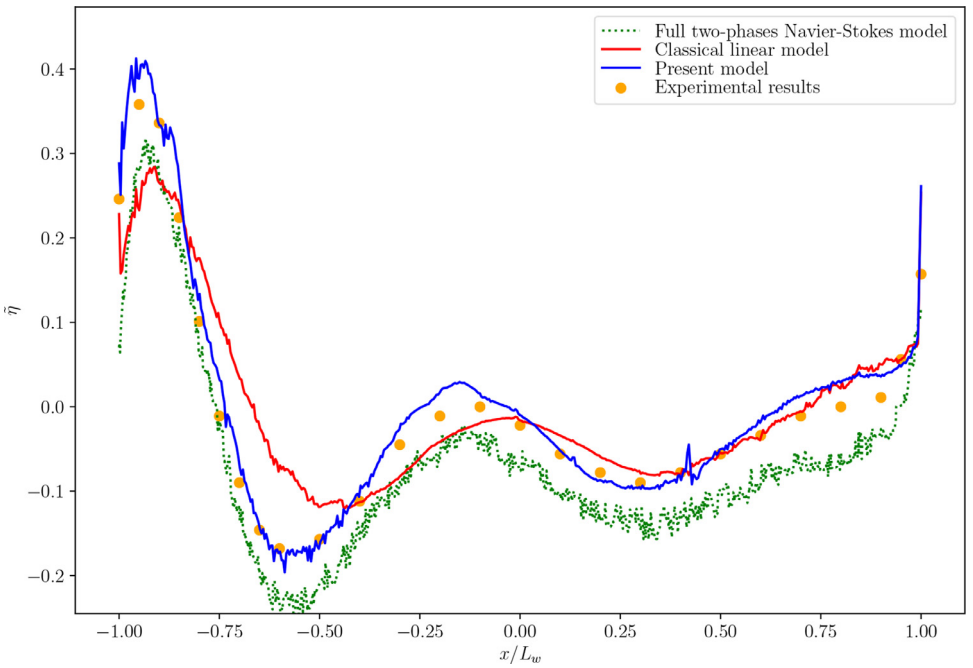

Fig. 7. Non-dimensional free surface elevation associated with the Kelvin wake generated by the Wigley hull with Fr = 0.267 (experimental results from Kajitani et al. [17] are depicted with orange dots, classical linear model with a red continuous line, Navier–Stokes results with a green dashed line, and results from the present model with a continuous blue line). (For interpretation of the references to colour in this figure legend, the reader is referred to the web version of this article.)

7.4. Numerical comparison with respect to the classical model

In Figs. 9–11, the free surface elevations (computed as it is described in Section 7.3) for the six experiments reported in Kajitani et al. [17] are compared with the numerical results of the proposed model and the classical linear model, (18), for three different meshes using linear finite elements. In all these numerical results, the free surface elevation is computed by means of the gradient of a continuous piecewise linear discretization of the velocity potential ϕ_a (see (34)), what would lead to a discontinuous piecewise constant approximation of η_a. To avoid these discontinuities per element, this gradient discretization is projected into a continuous piecewise linear discrete space, which is used to interpolate the free surface elevation at some points on the Wigley hull waterline.

In view of the numerical results reported in Figs. 9–11, the proposed model exhibits a robust behaviour to compute accurately the free surface elevation along the waterline for the six experiments (independently of the refinement type used in the mesh), while the classical linear model presents instabilities on the stern for some experiments in the coarse mesh.

Additionally, the resistance coefficients have been computed using for different meshes the classical, (18), and the proposed linear model. In all cases the resistance coefficient is given by

$$C_{PR} = \frac{R_p}{\frac{1}{2}\rho_f |\mathbf{v}^{ap}|^2 S}, \tag{35}$$

where S is the wetted surface area at rest defined by $S := 0.661 L_w(2D_w + B_w)$ (see Kajitani et al. [17]). Recall that B_w, L_w and D_w are the main dimensions of the hull (see Section 7.1), and the pressure resistance R_p is computed by

$$R_p = \int_{\Gamma_t^f} \mathbf{T}\mathbf{n} \cdot \frac{-\mathbf{v}^s}{|\mathbf{v}^s|}\, \mathrm{dA}_x = \int_{\Gamma_t^f} \pi\, \mathbf{n} \cdot \frac{\mathbf{v}^s}{|\mathbf{v}^s|}\, \mathrm{dA}_x = \int_{\Gamma_a^f} \pi_a \det \mathbf{F}_{Y_f} \mathbf{F}_{Y_f}^{-t} \mathbf{n}_a \cdot \mathbf{e}_1 \mathrm{dA}_z.$$

The ALE pressure field π_a is computed from the Bernoulli's equation written in Eulerian coordinates, as

$$\begin{aligned} \pi_a = (\pi)_a &= \left(\frac{\rho_f}{2} |\mathbf{v}^s|^2 - \frac{\rho_f}{2} |\operatorname{grad} \varphi|^2 - \rho_f g x_3 \right)_a \\ &= \frac{\rho_f}{2} |\mathbf{v}_a^s|^2 - \frac{\rho_f}{2} |\mathbf{F}_{Y_f}^{-t} \operatorname{grad}_a \varphi_a|^2 - \rho_f g \eta_a. \end{aligned}$$

Next, $\mathbf{F}_{Y_f}$ is approximated by the identity and η_a by z_3 leading to the formula,

$$R_p \approx \int_{\Gamma_a^f} \left(\frac{\rho_f}{2} |\mathbf{v}_a^s|^2 - \frac{\rho_f}{2} |\operatorname{grad}_a \varphi_a|^2 - \rho_f g z_3 \right) \mathbf{n}_a \cdot \mathbf{e}_1 \mathrm{dA}_z.$$

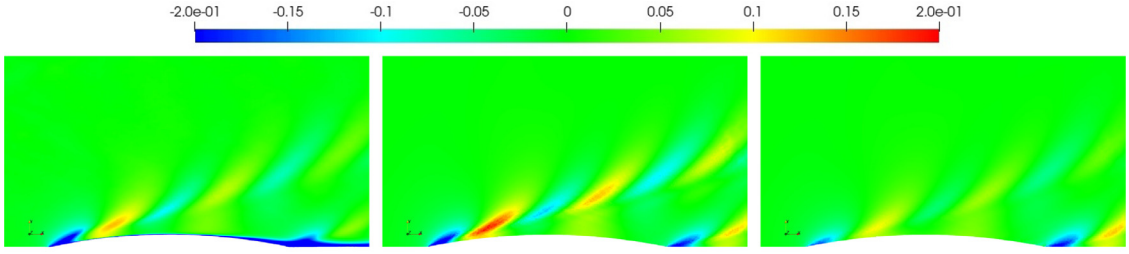

(a) First component of the velocity computed with the full Navier-Stokes model (b) First component of the velocity computed with the present model (c) First component of the velocity computed with the classical model

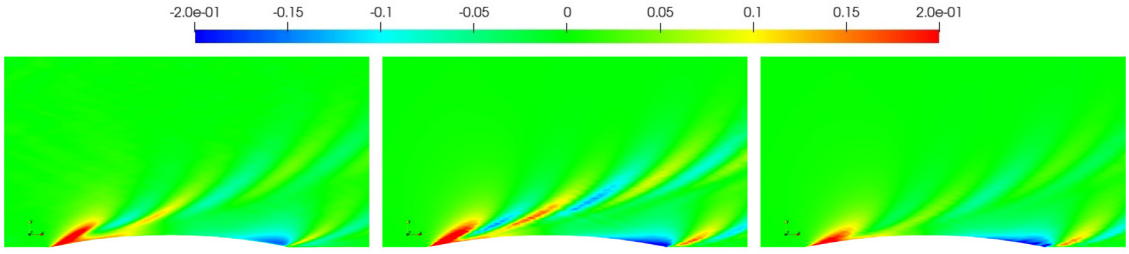

(d) Second component of the velocity computed with the full Navier-Stokes model (e) Second component of the velocity computed with the present model (f) Second component of the velocity computed with the classical model

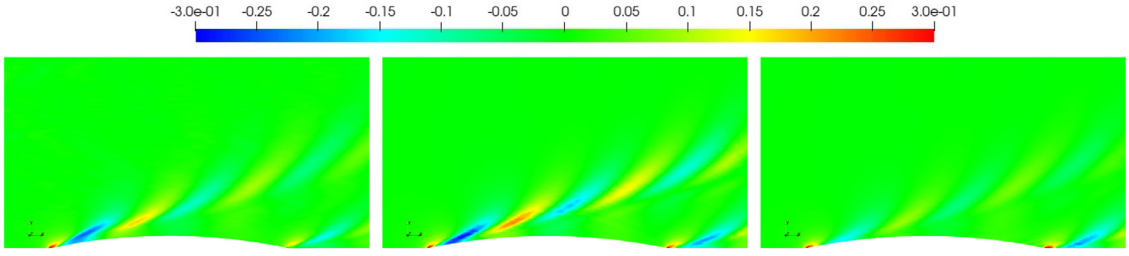

(g) Third component of the velocity computed with the full Navier-Stokes model (h) Third component of the velocity computed with the present model (i) Third component of the velocity computed with the classical model

Fig. 8. Numerical approximation of the velocity field for the Kelvin wake generated by the Wigley hull with Fr = 0.267 using the full Navier–Stokes model, the present model and the classical linear model (each row uses the same colour scale).

Table 1
Resistance coefficient (defined by (35)) computed with different models, meshes and Froude numbers using linear finite elements. The last row shows the experimental results for comparison purposes.

Model	Mesh	Fr			
		0.25	0.267	0.289	0.316
Present	Coarse mesh	6.997×10^{-4}	6.979×10^{-4}	1.046×10^{-3}	1.265×10^{-3}
Present	Fine mesh	7.178×10^{-4}	6.705×10^{-4}	1.082×10^{-3}	1.258×10^{-3}
Present	Very fine mesh	8.003×10^{-4}	6.722×10^{-4}	1.169×10^{-3}	1.373×10^{-3}
Classical	Coarse mesh	7.844×10^{-4}	8.525×10^{-4}	1.176×10^{-3}	1.376×10^{-3}
Classical	Fine mesh	7.632×10^{-4}	8.186×10^{-4}	1.228×10^{-3}	1.416×10^{-3}
Classical	Very fine mesh	9.568×10^{-4}	9.141×10^{-4}	1.360×10^{-3}	1.444×10^{-3}
Experimental results		9.41×10^{-4}	8.27×10^{-4}	1.221×10^{-3}	1.789×10^{-3}

This approximation could be the cause of the observed underestimation of the resistance coefficient. Table 1 shows the numerical approximation of the resistance coefficients, which are again compared with the experimental data reported in Kajitani et al. [17]. The resistance coefficient obtained from the full two-phase Navier–Stokes model was 1.054×10^{-3} in the case shown in Section 7.3 (Fr = 0.267).

Finally, the computational cost and the main characteristics of the three different meshes are shown in Table 2. The CPU time is averaged among the six experiments described above with different Froude numbers using a computer with 4 processors `Intel(R) Xeon(R) Gold 6126 CPU @ 2.60 GHz` and 380 GB of RAM. The numerical approximations have been computed sequentially and the linear discrete system has been calculated using a direct solver (MUMPS).

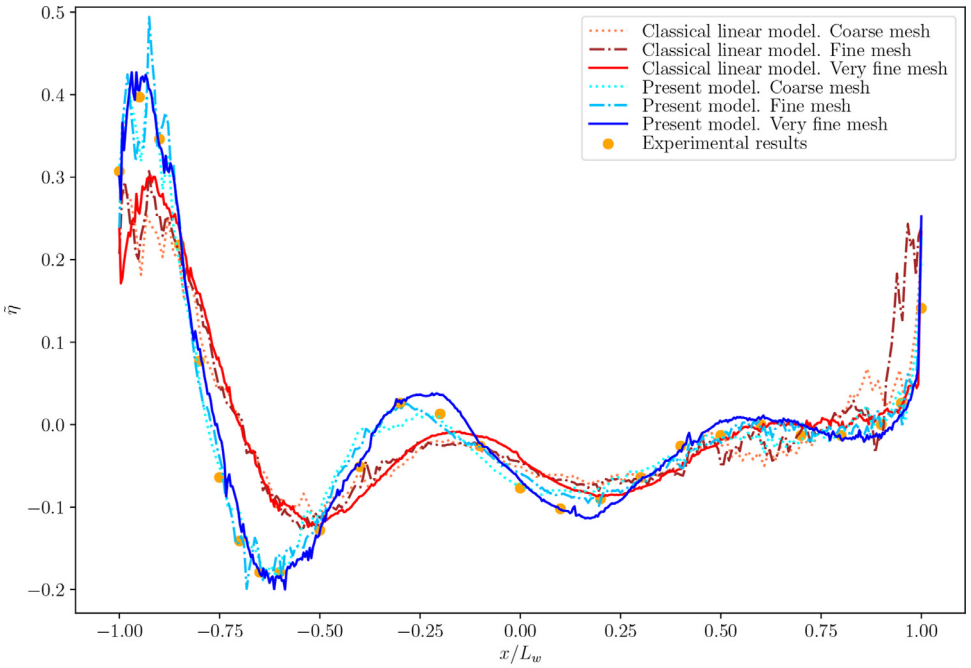

(a) Fr: 0.25

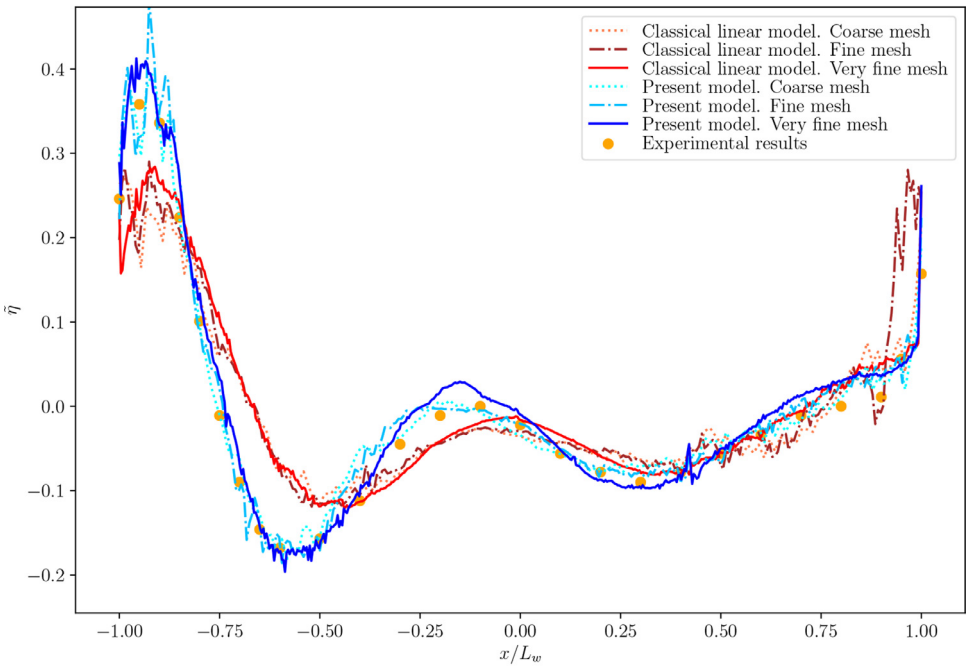

(b) Fr: 0.267

Fig. 9. Non-dimensional free surface elevation results at different Froude numbers (Fr = 0.25, 0.267) using the meshes shown in Fig. 4 and linear finite elements. They are compared with the experimental data (experimental results from [17] depicted with orange dots, classical linear model with lines in reddish colours and results from the present model with lines in bluish colours). (For interpretation of the references to colour in this figure legend, the reader is referred to the web version of this article.)

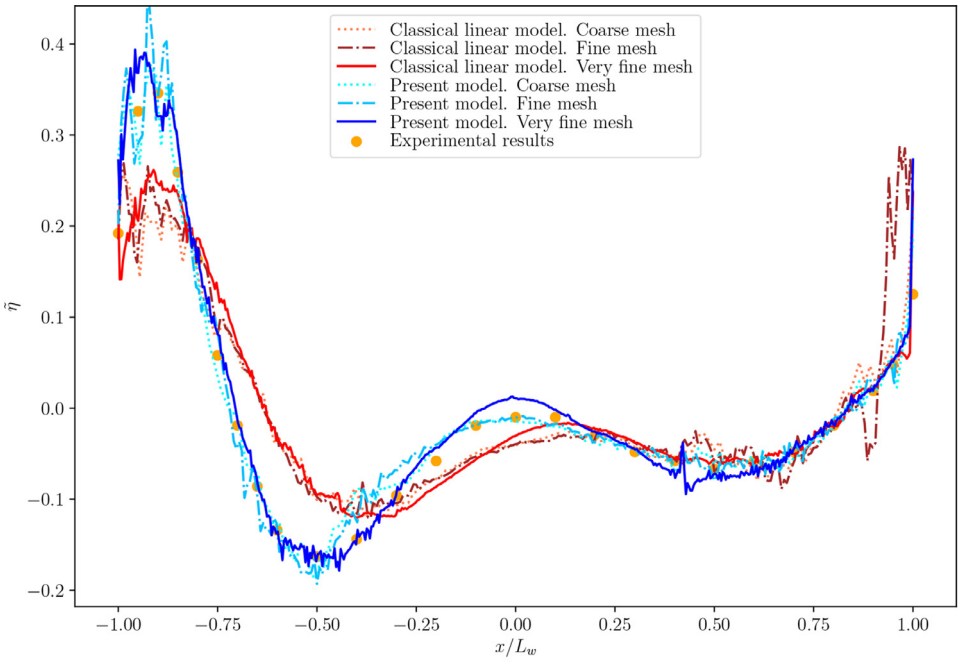

(a) Fr: 0.289

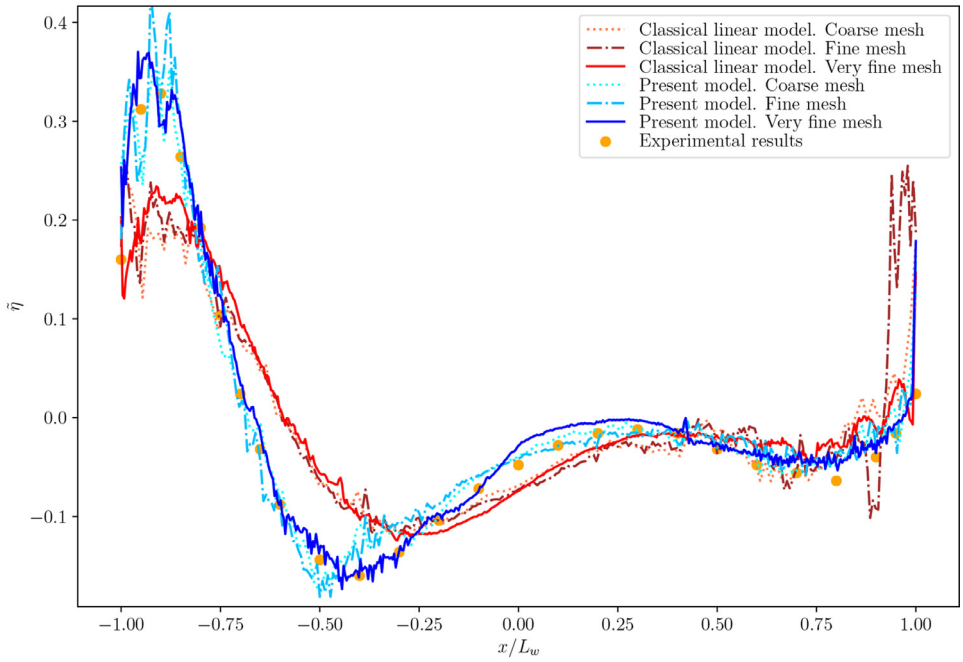

(b) Fr: 0.316

Fig. 10. Non-dimensional free surface elevation results at different Froude numbers (Fr = 0.289, 0.316) using the meshes shown in Fig. 4 and linear finite elements. They are compared with the experimental data (experimental results from Kajitani et al. [17] depicted with orange dots, classical linear model with lines in reddish colours and results from the present model with lines in bluish colours). (For interpretation of the references to colour in this figure legend, the reader is referred to the web version of this article.)

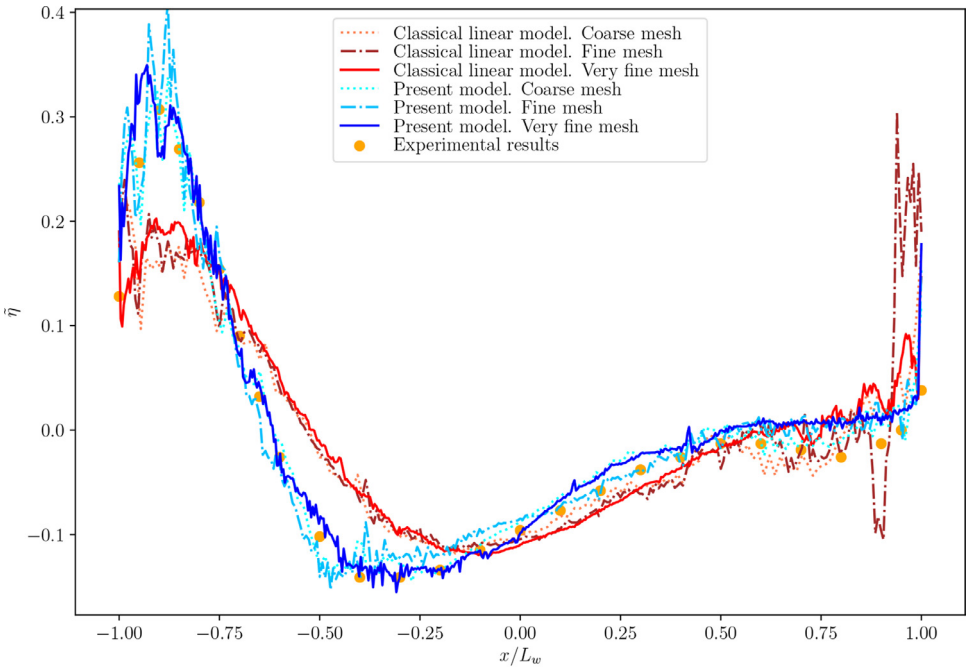

(a) Fr: 0.354

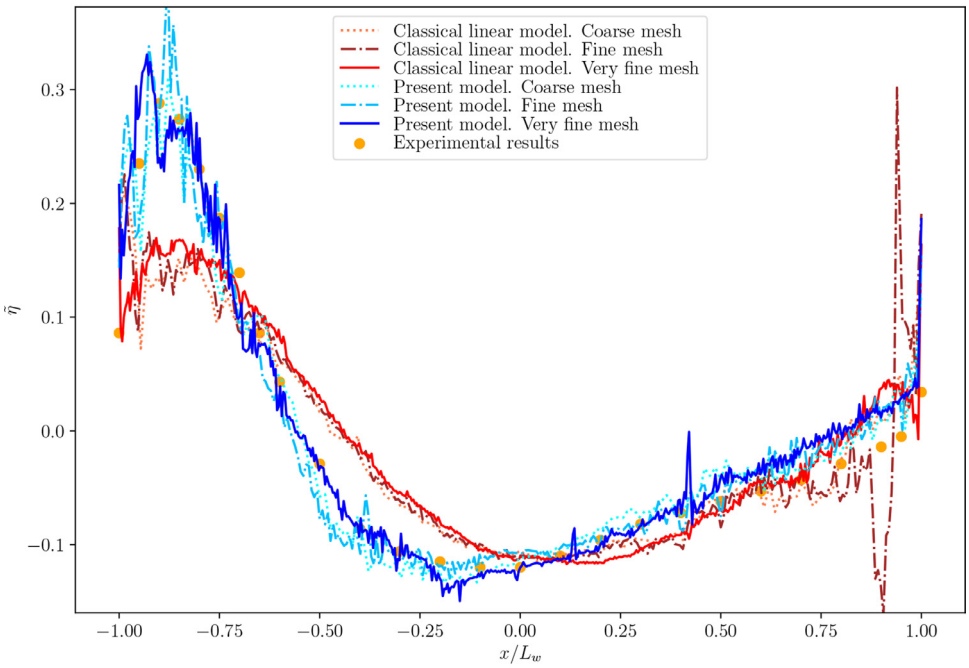

(b) Fr: 0.408

Fig. 11. Non-dimensional free surface elevation results at different Froude numbers (Fr = 0.354, 0.408) using the meshes shown in Fig. 4 and linear finite elements. They are compared with the experimental data (experimental results from Kajitani et al. [17] depicted with orange dots, classical linear model with lines in reddish colours and results from the present model with lines in bluish colours). (For interpretation of the references to colour in this figure legend, the reader is referred to the web version of this article.)

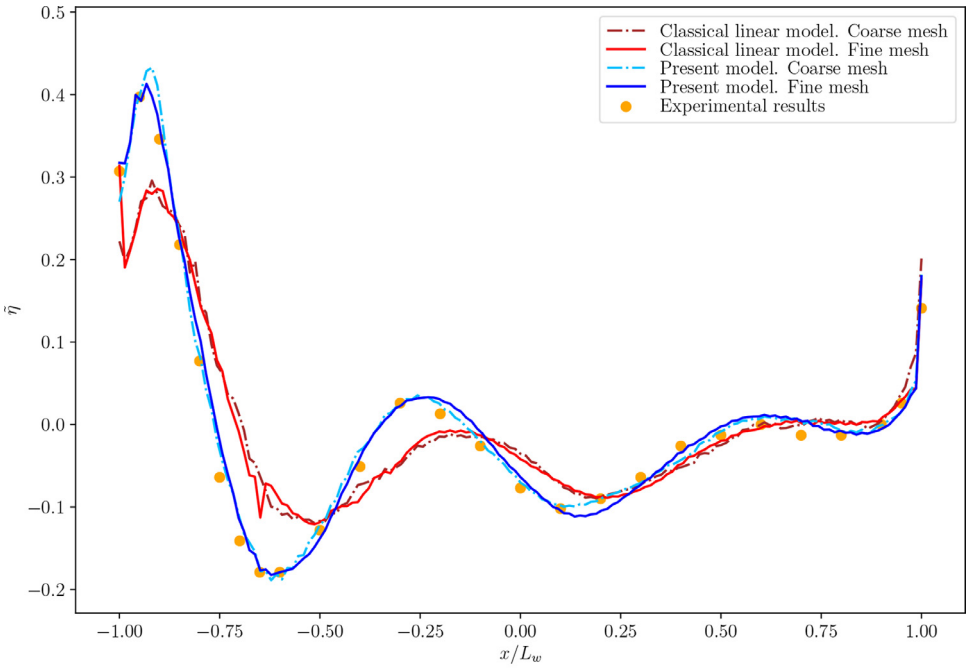

(a) Fr: 0.25

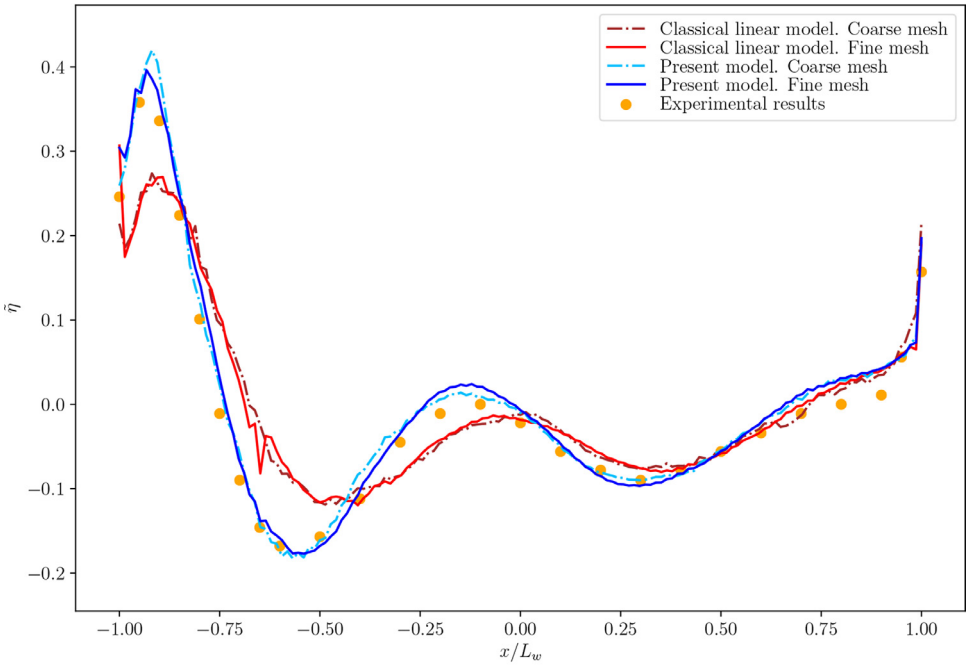

(b) Fr: 0.267

Fig. 12. Non-dimensional free surface elevation results at different Froude numbers (Fr = 0.25, 0.267) using the "coarse" mesh and the "fine" mesh shown in Fig. 4, and quadratic finite elements. They are compared with the experimental data (experimental results from Kajitani et al. [17] depicted with orange dots, classical linear model with lines in reddish colours and results from the present model with lines in bluish colours). (For interpretation of the references to colour in this figure legend, the reader is referred to the web version of this article.)

Table 2
Computational cost (CPU time) and mesh characteristics. The second column shows the average CPU time (among the six experiments described above with different Froude numbers). The first three meshes include the PML region but the reference mesh does not. The third and fourth columns show the number of vertices along the length and height of the wet surface of the Wigley, respectively. The fifth column shows the number of nodes (at midship) in the radial wake direction from the stern to the exterior boundary of the computational domain. The last column shows the number of tetrahedra of each mesh.

Mesh	Average time (s)	Vertices			Tetrahedra
		Length	Height	Wake	
Coarse	78	148	12	34	0.362×10^6
Fine	951	296	24	68	2.898×10^6
Very Fine	752	592	48	184	3.710×10^6
Reference	3153	296	24	586	1.771×10^7

Table 3
Resistance coefficient (defined by (35)) computed with different models, meshes and Froude numbers using quadratic finite elements. The last row shows the experimental results for comparison purposes.

Model	Mesh	Fr			
		0.25	0.267	0.289	0.316
Present	Coarse mesh	7.535×10^{-4}	6.761×10^{-4}	1.171×10^{-3}	1.332×10^{-3}
Present	Fine mesh	7.834×10^{-4}	6.852×10^{-4}	1.202×10^{-3}	1.363×10^{-3}
Classical	Coarse mesh	9.210×10^{-4}	9.376×10^{-4}	1.355×10^{-3}	1.360×10^{-3}
Classical	Fine mesh	9.511×10^{-4}	9.410×10^{-4}	1.409×10^{-3}	1.465×10^{-3}
Experimental results		9.41×10^{-4}	8.27×10^{-4}	1.221×10^{-3}	1.789×10^{-3}

The last columns in Table 2 contain information about the vertices distribution on the meshes (vertices on the length of the ship, nodes on the height of the ship, and nodes along the radial direction of the wake), and the number of tetrahedra.

7.4.1. Quadratic FE

To evaluate the sensitivity of the numerical results with respect to the finite element discretization, the velocity potential has been approximated based on quadratic finite elements. These numerical results have been compared with those obtained with linear finite elements. Figs. 12–14 show the free surface elevations (computed following the procedure described in Section 7.3) replicating the six experiments reported in Kajitani et al. [17]. Linear and quadratic approximations are compared using the proposed and the classical linear model, (18), for three different meshes. From this comparison, it can be concluded the use of a quadratic approximation smooths the high frequency spurious oscillations produced by the projection procedure used to compute the free elevation in the linear finite element approximation (described in Section 7.4). Finally, Table 3 shows the resistance coefficient, computed using (35), for the three different meshes and the classical and the proposed linear model.

8. Conclusions

A novel linear potential model for the free surface flow produced by the presence of a floating rigid body in motion have been derived by using an ALE formulation and a subsequent linearisation. The difficulties associated with its numerical resolution have been pointed out and discussed in detail: the convective term stated on the free surface boundary and the truncation of the unbounded physical domain where an outgoing radiation condition is imposed.

In order to overcome these difficulties, a new approach to upwind the convective term have been developed, which avoids a spurious numerical behaviour when it is combined with a PML technique. The use of a PML layer with a singular absorbing profile guarantee an accurate damping of the solution in the radial direction even when the computational domain is truncated near the floating body. The proposed methodology has been validated by comparing its numerical results with the available experimental data for the Wigley hull benchmark.

Currently, further work is being focused on the extension of the proposed numerical methodology based on a finite element discretization combined with a PML technique to solve numerically the unsteady problem, not only to simulate the Kelvin wake pattern but also to include incoming sea surface waves coupled with the rigid motion of the floating body.

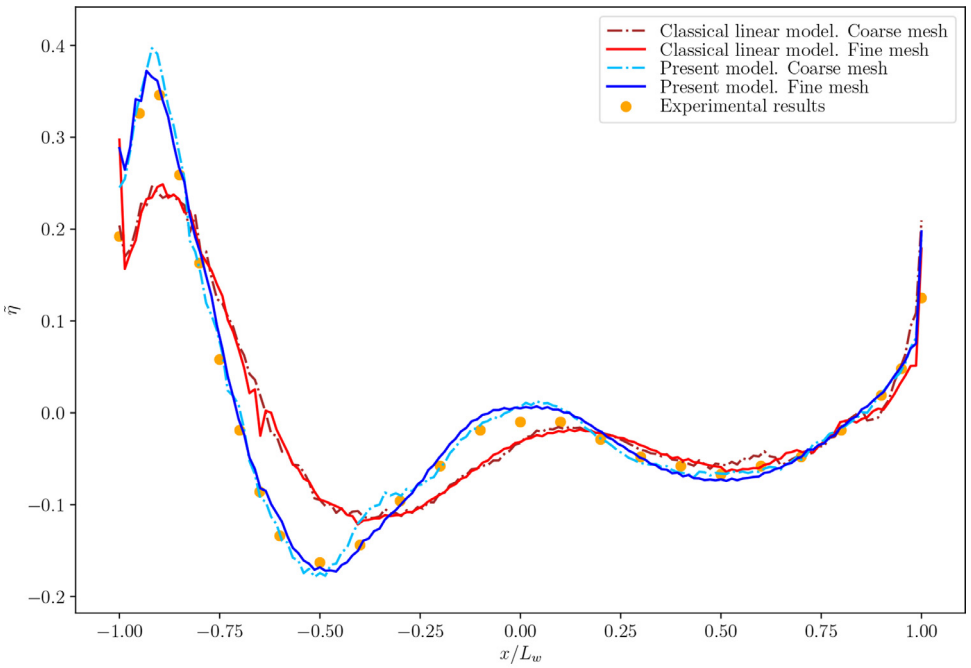

(a) Fr: 0.289

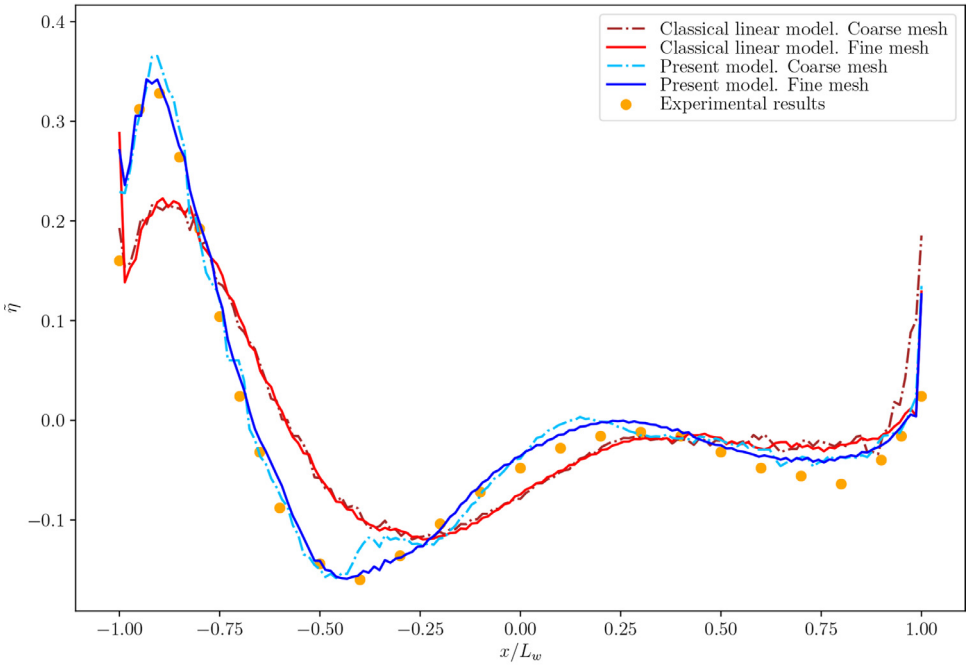

(b) Fr: 0.316

Fig. 13. Non-dimensional free surface elevation results at different Froude numbers (Fr = 0.289, 0.316) using the "coarse" mesh and the "fine" mesh shown in Fig. 4, and quadratic finite elements. They are compared with the experimental data (experimental results from Kajitani et al. [17] depicted with orange dots, classical linear model with lines in reddish colours and results from the present model with lines in bluish colours). (For interpretation of the references to colour in this figure legend, the reader is referred to the web version of this article.)

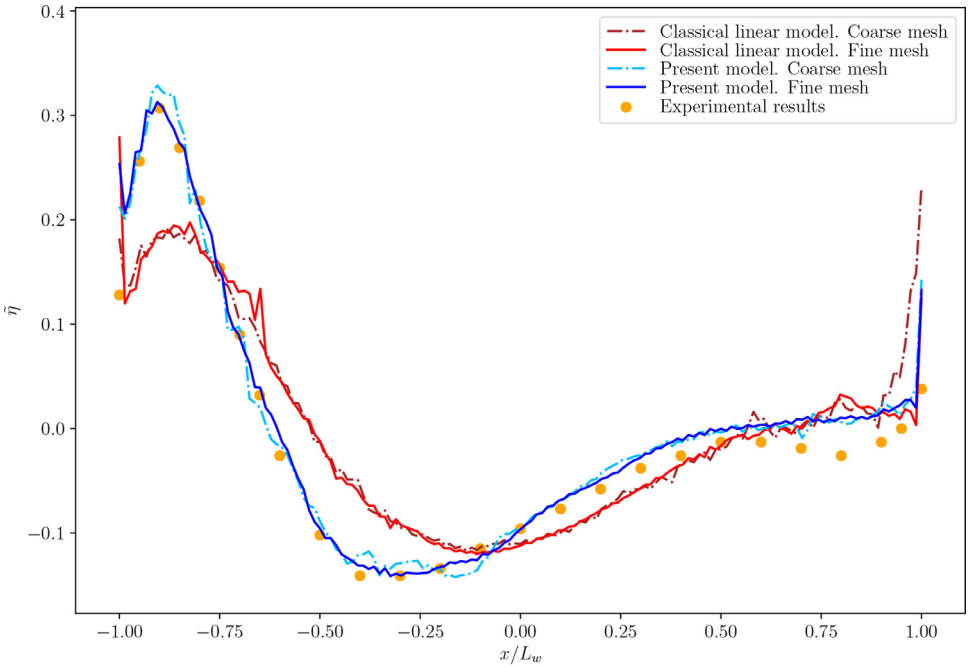

(a) Fr: 0.354

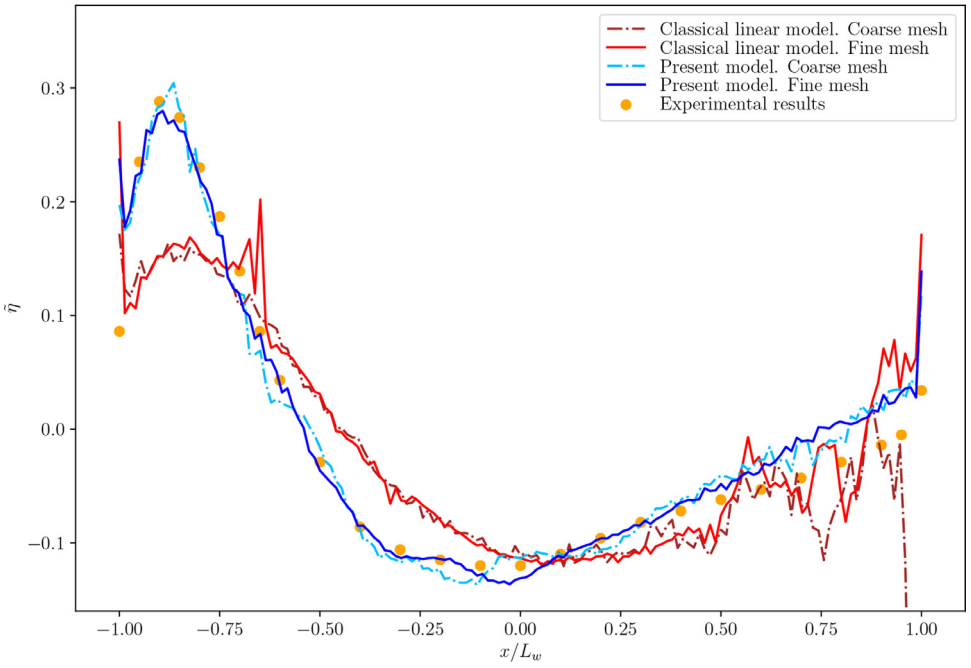

(b) Fr: 0.408

Fig. 14. Non-dimensional free surface elevation results at different Froude numbers (Fr = 0.354, 0.408) using the "coarse" mesh and the "fine" mesh shown in Fig. 4, and quadratic finite elements. They are compared with the experimental data (experimental results from Kajitani et al. [17] depicted with orange dots, classical linear model with lines in reddish colours and results from the present model with lines in bluish colours). (For interpretation of the references to colour in this figure legend, the reader is referred to the web version of this article.)

Acknowledgements

The first two authors have been partially supported by FSE Galicia 2014-2020 and Xunta de Galicia under grant ED481A-2018/212; by Xunta de Galicia & ERDF under grant ED431C 2021/15 and by MICINN/Agencia Estatal de Investigacin & ERDF under the research project MTM2017-86459-R. The third author has been supported by MICINN & ERDF projects MTM2017-82724-R, PID2019-108584RB-I00, and also by ED431C 2018/33 - M2NICA (Xunta de Galicia & ERDF) and ED431G 2019/01 - CITIC (Xunta de Galicia & ERDF).

Appendix A. Proof of Theorem 3.1

Before being in a position to show Theorem 3.1, the material description of a spatial field must be defined explicitly. It is also necessary to introduce two auxiliary lemmas about the relation between the gradients of motions Y_f and Z_f.

Definition A.1. Let $f:\mathcal{T}\to\mathbb{R}$ be a spatial (or Eulerian) field and $g:\mathcal{A}\times\mathbb{R}^+\to\mathbb{R}$ be a field defined in the AL configuration. Their respective material descriptions are defined by

$$f_m(p,t):=f(X_f(p,t),t)\quad\text{ and }\quad g_m(p,t):=g(Z_f(p,t),t),$$

where X_f denotes the total motion of the fluid and Z_f the underlying motion used in the AL description.

Besides, recall that subscript a denotes the *AL* description (see Section 3).

Lemma A.1. *Let X_f be a motion, Y_f and Z_f be the decomposition described in Section 3, and let $\mathbf{F}_{X_f}$, $\mathbf{F}_{Y_f}$ and $\mathbf{F}_{Z_f}$ denote their respective gradients. Then, it holds*

$$\left(\mathbf{F}_{Z_f}^{-t}\right)_a\left(-\left(\frac{\partial\mathbf{F}_{X_f}^t}{\partial t}\right)_a\mathbf{F}_{Y_f}^{-t}+\left(\frac{\partial\mathbf{F}_{Z_f}^t}{\partial t}\right)_a\right)=-\left(\frac{\partial\left(\mathbf{F}_{Y_f}^t\right)_m}{\partial t}\right)_a\mathbf{F}_{Y_f}^{-t}.$$

Proof. Firstly, since $X(p,t)=Y(Z(p,t),t)$, a straightforward use of the chain rule leads to

$$\frac{\partial\mathbf{F}_{X_f}^t}{\partial t}=\frac{\partial}{\partial t}\left(\mathbf{F}_{Z_f}^t\left(\mathbf{F}_{Y_f}^t\right)_m\right)=\frac{\partial\mathbf{F}_{Z_f}^t}{\partial t}\left(\mathbf{F}_{Y_f}^t\right)_m+\mathbf{F}_{Z_f}^t\frac{\partial\left(\mathbf{F}_{Y_f}^t\right)_m}{\partial t},\tag{A.1}$$

and then, replacing the time derivative of $\mathbf{F}_{X_f}^t$ by the expression written above in the left-hand side of (A.1), it holds

$$\begin{aligned}&\left(\mathbf{F}_{Z_f}^{-t}\right)_a\left(-\left(\frac{\partial\mathbf{F}_{X_f}^t}{\partial t}\right)_a\mathbf{F}_{Y_f}^{-t}+\left(\frac{\partial\mathbf{F}_{Z_f}^t}{\partial t}\right)_a\right)\\&=\left(\mathbf{F}_{Z_f}^{-t}\right)_a\left[-\left(\frac{\partial\mathbf{F}_{Z_f}^t}{\partial t}\right)_a-\left(\mathbf{F}_{Z_f}^t\right)_a\left(\frac{\partial\left(\mathbf{F}_{Y_f}^t\right)_m}{\partial t}\right)_a\mathbf{F}_{Y_f}^{-t}+\left(\frac{\partial\mathbf{F}_{Z_f}^t}{\partial t}\right)_a\right]=-\left(\frac{\partial\left(\mathbf{F}_{Y_f}^t\right)_m}{\partial t}\right)_a\mathbf{F}_{Y_f}^{-t}.\end{aligned}$$

□

Lemma A.2. *Let φ be a potential field associated with the irrotational motion X_f of an incompressible and inviscid fluid such that $\operatorname{grad}\varphi(x,t)=\mathbf{v}(x,t):=\dot{X}_f(P_{X_f}(x,t),t)$, where P_{X_f} denotes the reference mapping of X_f. Let Y_f and Z_f be the decomposition of motion X_f described in Section 3, and $\mathbf{F}_{Y_f}$, $\mathbf{F}_{Z_f}$ and $\mathbf{F}_{X_f}$ denote their respective gradients. Then, it holds*

$$\left((\operatorname{grad}\varphi)^{\cdot}\right)_a=\mathbf{F}_{Y_f}^{-t}\left[-\left(\frac{\partial\left(\mathbf{F}_{Y_f}^t\right)_m}{\partial t}\right)_a\mathbf{F}_{Y_f}^{-t}\operatorname{grad}_a\varphi_a+\operatorname{grad}_a\frac{\partial\varphi_a}{\partial t}+\mathbf{grad}_a\operatorname{grad}_a\varphi_a\mathbf{d}_a\right].$$

Proof. Firstly, it is straightforward to check that

$$\left((\operatorname{grad}\varphi)^{\cdot}\right)_a=\left(((\operatorname{grad}\varphi)_m)^{\cdot}\right)_a,\qquad\frac{\partial\mathbf{F}_{X_f}^{-t}}{\partial t}=-\mathbf{F}_{X_f}^{-t}\frac{\partial\mathbf{F}_{X_f}^t}{\partial t}\mathbf{F}_{X_f}^{-t}.$$

Additionally, using the chain of rule, $(\operatorname{grad}\varphi)_m=\mathbf{F}_{X_f}^{-t}\operatorname{grad}_m\varphi_m$ and $\operatorname{grad}_m\varphi_m=\mathbf{F}_{Z_f}^t(\operatorname{grad}_a\varphi_a)_m$. Hence,

$$\begin{aligned}((\operatorname{grad}\varphi)_m)^{\cdot}&=\frac{\partial}{\partial t}(\operatorname{grad}\varphi)_m=\frac{\partial}{\partial t}\left(\mathbf{F}_{X_f}^{-t}\operatorname{grad}_m\varphi_m\right)=\frac{\partial\mathbf{F}_{X_f}^{-t}}{\partial t}\operatorname{grad}_m\varphi_m+\mathbf{F}_{X_f}^{-t}\frac{\partial}{\partial t}(\operatorname{grad}_m\varphi_m)\\&=\mathbf{F}_{X_f}^{-t}\left[-\frac{\partial\mathbf{F}_{X_f}^t}{\partial t}\mathbf{F}_{X_f}^{-t}\mathbf{F}_{Z_f}^t(\operatorname{grad}_a\varphi_a)_m+\frac{\partial}{\partial t}\left(\mathbf{F}_{Z_f}^t(\operatorname{grad}_a\varphi_a)_m\right)\right]\end{aligned}$$

$$= \mathbf{F}_{X_f}^{-t}\left[-\frac{\partial \mathbf{F}_{X_f}^{t}}{\partial t}\left(\mathbf{F}_{Y_f}^{-t}\right)_m (\mathrm{grad}_a\,\varphi_a)_m + \frac{\partial \mathbf{F}_{Z_f}^{t}}{\partial t}(\mathrm{grad}_a\,\varphi_a)_m + \mathbf{F}_{Z_t}^{t}\frac{\partial}{\partial t}(\mathrm{grad}_a\,\varphi_a)_m\right]$$

$$= \left(\mathbf{F}_{Y_f}^{-t}\right)_m\left[\mathbf{F}_{Z_f}^{-t}\left(-\frac{\partial \mathbf{F}_{X_f}^{t}}{\partial t}\left(\mathbf{F}_{Y_f}^{-t}\right)_m + \frac{\partial \mathbf{F}_{Z_f}^{t}}{\partial t}\right)(\mathrm{grad}_a\,\varphi_a)_m + \frac{\partial}{\partial t}(\mathrm{grad}_a\,\varphi_a)_m\right], \tag{A.2}$$

because $\mathbf{F}_{X_f}^{-t}\mathbf{F}_{Z_f}^{t} = \left(\mathbf{F}_{Y_f}^{-t}\right)_m$ from $\mathbf{F}_{X_f}(p,t) = \mathbf{F}_{Y_f}(Z_f(p,t),t)\mathbf{F}_{Z_f}(p,t)$ which, in turn, is direct from (6). Moreover, working with the last term of the expression,

$$\frac{\partial}{\partial t}(\mathrm{grad}_a\,\varphi_a)_m = \left(\frac{\partial}{\partial t}(\mathrm{grad}_a\,\varphi_a)\right)_m + (\mathbf{grad}_a\,\mathrm{grad}_a\,\varphi_a)_m\frac{\partial Z_f}{\partial t} = \left(\mathrm{grad}_a\,\frac{\partial \varphi_a}{\partial t}\right)_m + (\mathbf{grad}_a\,\mathrm{grad}_a\,\varphi_a)_m\mathbf{d}.$$

Then, the replacement of the expression above in the last term of (A.2) leads to

$$((\mathrm{grad}\,\varphi)_m)^{\cdot} = \left(\mathbf{F}_{Y_f}^{-t}\right)_m\left[\mathbf{F}_{Z_f}^{-t}\left(-\frac{\partial \mathbf{F}_{X_f}^{t}}{\partial t}\left(\mathbf{F}_{Y_f}^{-t}\right)_m + \frac{\partial \mathbf{F}_{Z_f}^{t}}{\partial t}\right)(\mathrm{grad}_a\,\varphi_a)_m + \left(\mathrm{grad}_a\,\frac{\partial \varphi_a}{\partial t}\right)_m + (\mathbf{grad}_a\,\mathrm{grad}_a\,\varphi)_m\mathbf{d}\right]$$

and hence, its AL description is given by

$$\left((\mathrm{grad}\,\varphi)^{\cdot}\right)_a = \mathbf{F}_{Y_f}^{-t}\left[(\mathbf{F}_{Z_f}^{-t})_a\left(-\left(\frac{\partial \mathbf{F}_{X_f}^{t}}{\partial t}\right)_a\mathbf{F}_{Y_f}^{-t} + \left(\frac{\partial \mathbf{F}_{Z_f}^{t}}{\partial t}\right)_a\right)\mathrm{grad}_a\,\varphi_a + \mathrm{grad}_a\,\frac{\partial \varphi_a}{\partial t} + \mathbf{grad}_a\,\mathrm{grad}_a\,\varphi_a\mathbf{d}_a\right].$$

The result follows by using Lemma A.1. □

Now the proof of Theorem 3.1 can be derived straightforwardly as follows.

Proof. Firstly, the motion equation (1) in AL variables becomes

$$\rho_f\left((\mathrm{grad}\,\varphi)^{\cdot}\right)_a + (\mathrm{grad}\,\pi)_a = -\left(\mathrm{grad}\left(\rho_f g x_3\right)\right)_a$$

and, equivalently,

$$\rho_f\left((\mathrm{grad}\,\varphi)^{\cdot}\right)_a + \mathbf{F}_{Y_f}^{-t}\,\mathrm{grad}_a\,\pi_a = -\mathbf{F}_{Y_f}^{-t}\,\mathrm{grad}_a\left(\rho_f g\eta_a\right).$$

Then, using Lemma A.2,

$$\rho_f\mathbf{F}_{Y_f}^{-t}\left[-\left(\frac{\partial\left(\mathbf{F}_{Y_f}^{t}\right)_m}{\partial t}\right)_a\mathbf{F}_{Y_f}^{-t}\,\mathrm{grad}_a\,\varphi_a + \mathrm{grad}_a\,\frac{\partial \varphi_a}{\partial t} + \mathbf{grad}_a\,\mathrm{grad}_a\,\varphi_a\mathbf{d}_a\right] + \mathbf{F}_{Y_f}^{-t}\,\mathrm{grad}_a\,\pi_a = -\mathbf{F}_{Y_f}^{-t}\,\mathrm{grad}_a\left(\rho_f g\eta_a\right),$$

and multiplying by $\mathbf{F}_{Y_f}^{t}$ both sides of the equation above, it holds

$$-\rho_f\left(\frac{\partial\left(\mathbf{F}_{Y_f}^{t}\right)_m}{\partial t}\right)_a\mathbf{F}_{Y_f}^{-t}\,\mathrm{grad}_a\,\varphi_a + \rho_f\,\mathbf{grad}_a\,\mathrm{grad}_a\,\varphi_a\mathbf{d}_a + \rho_f\,\mathrm{grad}_a\,\frac{\partial \varphi_a}{\partial t} + \mathrm{grad}_a\,\pi_a + \mathrm{grad}_a\left(\rho_f g\eta_a\right) = \mathbf{0}.$$

Finally, the result is obtained from the previous equation combined with

$$\left(\frac{\partial\left(\mathbf{F}_{Y_f}^{t}\right)_m}{\partial t}\right)_a = \left(\mathbf{grad}_a\,\frac{\partial \mathbf{u}}{\partial t}\right)^t + \mathbf{grad}_a(\mathbf{grad}_a\,\mathbf{u})^t\mathbf{d}_a,$$

where $\mathbf{u}(z,t) := Y_f(z,t) - z$. □

Appendix B. Perfectly matched layer

The numerical computation of any hydrodynamic problem stated in an unbounded domain requires the use of special techniques either to reformulate it in a new bounded domain (as it can be made by means of integral equations on the boundary of a floating bounded body) or to truncate the original unbounded fluid domain with some damping methodologies, which do not distort excessively the solution with spurious errors coming from this artificial exterior boundary. Among the latter methods, the introduction of artificial damping terms or the so-called numerical beaches (see Kim et al. [26]) are widely used in hydrodynamics. However, during the last two decades, the Perfectly Matched Layer (PML) technique introduced by Berenger [9] has been successfully applied to a large variety of models involving wave propagation phenomena and stated in unbounded domains (see for instance Karperaki et al. [27]).

In the PML methodology, instead of adding some extra damping terms to the original model in the PML region surrounding the physical domain of interest, the partial derivatives of the governing equations are replaced by new complex-stretched

derivatives in such a manner that the solution of the original model ϕ matches perfectly the solution $\hat{\phi}$ inside the PML region. More precisely, in the present manuscript, the PML region is located in a cylindrical annulus surrounding the physical domain of interest between $r = R$ and $r = R_\infty$, so the radial coordinate r and the partial derivative with respect to r are replaced formally in the governing equations stated in the PML region as follows:

$$r \text{ is replaced by } \hat{r} \quad \text{and} \quad \frac{\partial}{\partial r} \text{ is replaced by } \frac{\partial}{\partial \hat{r}} = \frac{1}{\gamma}\frac{\partial}{\partial r},$$

where

$$\hat{r}(r) = r + \frac{i}{\omega_p}\int_R^r \sigma_r(s)\,\mathrm{d}s \quad \text{and} \quad \gamma(r) = 1 + \frac{i}{\omega_p}\sigma_r(r).$$

To illustrate how this complex stretching of coordinates is affecting the solution of the model with a PML layer, it is assumed here, for simplicity, that the solution of the unknown potential in the original model is given by $\phi(r,\theta,z) = \mathrm{Re}(\psi(\theta,z)e^{ik_w r})$, where the value of k_w determines the overall wavelength of the wake pattern. Obviously, a simple truncation without PML regions, imposing $\phi = 0$ on the truncation boundary, would introduce some spurious errors in the computed solution, since the potential ϕ is far from being null on the exterior boundary $r = R_\infty$. However, when the PML technique is used, the solution of the complex-stretched model in the PML region is given by

$$\hat{\phi}(r,\theta,z) = \phi\big(\hat{r}(r),\theta,z\big) = \mathrm{Re}\big(\psi(\theta,z)e^{ik_w\hat{r}(r)}\big) = \mathrm{Re}\big(\psi(\theta,z)e^{ik_w r}\big)e^{-\frac{k_w}{\omega_p}\int_R^r \sigma_r(s)\,\mathrm{d}s}.$$

The last factor in the expression above introduces a damping effect on the PML solution $\hat{\phi}$, which forces an exponential decreasing of the solution inside the PML region. In particular, since $\sigma_r(r)$ is a positive increasing function with an asymptote at $r = R_\infty$ (see Bermúdez et al. [12]), the PML solution satisfies $\hat{\phi} = 0$ on the exterior boundary of the PML region. Consequently, thanks to the use of this PML technique, it is possible to truncate the unbounded original domain with a simple homogeneous Dirichlet condition without introducing spurious errors in the solution ϕ computed in the physical domain of interest. The additional computational cost associated with the PML technique lies in the fact that the original governing equations in the physical domain of interest and the complex-stretched governing equations in the PML region have to be solved simultaneously using complex arithmetic.

B1. Kelvin wake angle θ_p

The setting of the PML absorption profile benefits from a prior knowledge of the Kelvin wake angle, θ_p. However, the approximation described in Remark 6.2 could be inaccurate especially at high Froude numbers. In what follows, the sensitivity of the numerical results obtained with the PML technique are analysed with respect to the angle θ_p.

First, angular frequency ω and angle θ_p are involved in the dispersion equation (25), which relates frequency and wavenumber in a classical planewave analysis (see Remark 6.2). Hence, the frequency can be read as a continuous function depending on the angle $\omega_p = \omega(\theta_p)$, which is defined implicitly using (25). Second, the PML governing equation depends on the chosen absorption profile (32), and hence it depends strongly on the complex-valued expressions used to define its coefficients:

$$\begin{aligned}
\hat{r}(r) &:= r + \frac{i}{\omega}\int_R^r \sigma_r(s)\,\mathrm{d}s = r + i\frac{\sigma_0}{\omega(\theta_p)}\int_R^r \left(\frac{1}{R_\infty - s} - \frac{1}{R_\infty - R}\right)ds,\\
\gamma(r) &= 1 + \frac{i}{\omega}\sigma_r(r) = 1 + i\frac{\sigma_0}{\omega(\theta_p)}\left(\frac{1}{R_\infty - r} - \frac{1}{R_\infty - R}\right),\\
\hat{\gamma}(r) &= 1 + \frac{i}{\omega}\sigma_\theta(r) = 1 + i\frac{\sigma_0}{\omega(\theta_p)}\frac{1}{r}\int_R^r \left(\frac{1}{R_\infty - s} - \frac{1}{R_\infty - R}\right)ds.
\end{aligned}$$

A direct inspection of these expressions show that all the coefficients written above depends on the ratio $\sigma_0/\omega(\theta_p)$. Therefore, an inaccurate approximation of angle θ_p, and subsequently of $\omega(\theta_p)$, can be balanced in the optimization of the parameter value σ_0 for a fixed Froude number.

However, if σ_0 is fixed for a variety of Froude numbers then the accuracy of the PML technique could be affected. To show the sensitivity of the numerical results with respect to the estimation of the wake angle θ_p and the Froude number Fr, the numerical approximations of the proposed model have been computed using a fixed PML value $\sigma_0 = 0.02$ for a number of scenarios, where different Froude numbers are considered, namely, $\mathrm{Fr} = 0.25,\ 0.316,\ 0.408$, and the reference value of $\theta_p = 0.6155$ is varied in a range from -40% to $+40\%$. Table B.4 shows the relative difference (using an analogous expression to (33)) between the numerical approximation computed with $\theta_p = 0.6155$ (see Remark 6.2) and the modified values of θ_p. It can be observed that the relative differences between the reference solution and the other numerical approximations are not significantly different, what shows the robustness of the PML accuracy with respect to the estimation of θ_p and the variability of the Froude number.

Table B1
Relative difference between the numerical approximation computed with the reference value $\theta_p = 0.6155$ and with the approximation obtained using other wake angle θ_p, which is varied in a range from −40% to +40% from the reference value. Each row shows the numerical results associated with different Froude numbers.

Fr	Range for varying θ_p from 0.6155					
	−40%	−20%	−10%	+10%	+20%	+40%
0.25	4.00×10^{-6}	2.21×10^{-6}	1.16×10^{-6}	1.25×10^{-6}	2.59×10^{-6}	5.48×10^{-6}
0.316	1.99×10^{-5}	1.11×10^{-5}	5.84×10^{-6}	6.41×10^{-6}	1.34×10^{-5}	2.90×10^{-5}
0.408	1.42×10^{-5}	7.65×10^{-6}	3.92×10^{-6}	4.03×10^{-6}	8.10×10^{-6}	1.61×10^{-5}

References

[1] J.N. Newman, Marine Hydrodynamics, ninth ed., The MIT Press, Cambridge, 1999.
[2] O.K. Kinaci, O.F. Sukas, S. Bal, Prediction of wave resistance by a Reynolds-averaged Navier–Stokes equation–based computational fluid dynamics approach, Proc. Inst. Mech. Eng., Part M 230 (3) (2016) 531–548.
[3] N. Kuznetsov, V. Maz'ya, B. Vainberg, Linear Water Waves: A Mathematical Approach, Cambridge University Press, Cambridge, 2004.
[4] J. Sarrate, A. Huerta, J. Donea, Arbitrary Lagrangian-Eulerian formulation for fluid-rigid body interaction, Comput. Methods Appl. Mech. Eng. 190 (24–25) (2001) 3171–3188.
[5] M. Benítez, A. Bermúdez, Pure Lagrangian and semi-Lagrangian finite element methods for the numerical solution of Navier–Stokes equations, Appl. Numer. Math. 95 (2015) 62–81.
[6] M. Shahjada Tarafder, K. Suzuki, Numerical calculation of free-surface potential flow around a ship using the modified Rankine source panel method, Ocean Eng. 35 (5) (2008) 536–544.
[7] X. Yu, S. Li, C. Hsiung, Numerical analysis of nonlinear ship wavemaking problem by the coupled element method, in: Proceedings of the Sixth International Conference on Numerical Ship Hydrodynamics, National Academies Press, 1994.
[8] N. Giuliani, A. Mola, L. Heltai, L. Formaggia, FEM SUPG stabilisation of mixed isoparametric BEMs: application to linearised free surface flows, Eng. Anal. Bound. Elem. 59 (2015) 8–22.
[9] J.-P. Berenger, A perfectly matched layer for the absorption of electromagnetic waves, J. Comput. Phys. 114 (2) (1994) 185–200.
[10] S. Abarbanel, D. Gottlieb, J.S. Hesthaven, Well-posed perfectly matched layers for advective acoustics, J. Comput. Phys. 154 (2) (1999) 266–283.
[11] Q. Qi, T.L. Geers, Evaluation of the perfectly matched layer for computational acoustics, J. Comput. Phys. 139 (1) (1998) 166–183.
[12] A. Bermúdez, L. Hervella-Nieto, A. Prieto, R. Rodríguez, An optimal perfectly matched layer with unbounded absorbing function for time-harmonic acoustic scattering problems, J. Comput. Phys. 223 (2) (2007) 469–488.
[13] G. Cohen, S. Imperiale, Perfectly matched layer with mixed spectral elements for the propagation of linearized water waves, Commun. Comput. Phys. 11 (2) (2012) 285–302.
[14] A.N. Brooks, T.J. Hughes, Streamline upwind/Petrov–Galerkin formulations for convection dominated flows with particular emphasis on the incompressible navier-Stokes equations, Comput. Methods Appl. Mech. Eng. 32 (1–3) (1982) 199–259.
[15] O. Pironneau, Finite Element Methods for Fluids, Wiley Chichester, 1989.
[16] A. Mola, L. Heltai, A. Desimone, A stable and adaptive semi-Lagrangian potential model for unsteady and nonlinear ship-wave interactions, Eng. Anal. Bound. Elem. 37 (2012) 128–143.
[17] H. Kajitani, H. Miyata, M. Ikehata, H. Tanaka, H. Adachi, M. Namimatsu, S. Ogiwara, The Summary of the Cooperative Experiment on Wigley Parabolic Model in Japan, Technical Report, University of Tokyo (Japan), 1983.
[18] M.E. Gurtin, An Introduction to Continuum Mechanics, Academic Press, New York, 1982.
[19] L. Landau, E. Lifshitz, Fluid Mechanics, second ed., Pergamon Press, Oxford, 1987.
[20] D.V. Trenev, Spatial Scaling for the Numerical Approximation of Problems on Unbounded Domains, 2009 Ph.D. thesis.
[21] W.C. Chew, W.H. Weedon, A 3D perfectly matched medium from modified Maxwell's equations with stretched coordinates, Microw. Opt. Technol. Lett. 7 (13) (1994) 599–604.
[22] M.S. Alnæs, J. Blechta, J. Hake, A. Johansson, B. Kehlet, A. Logg, C. Richardson, J. Ring, M.E. Rognes, G.N. Wells, The FEniCS project version 1.5, Arch. Numer. Softw. 3 (100) (2015) 9–23.
[23] A. Logg, K.-A. Mardal, G.N. Wells, et al., Automated Solution of Differential Equations by the Finite Element Method, Springer, 2012.
[24] D.C. Wilcox, Turbulence Modeling for CFD, third ed., DCW Industries, La Cañada, CA, 2006.
[25] C. Hirt, B. Nichols, Volume of fluid (VOF) method for the dynamics of free boundaries, J. Comput. Phys. 39 (1) (1981) 201–225.
[26] M.W. Kim, W. Koo, S.Y. Hong, Numerical analysis of various artificial damping schemes in a three-dimensional numerical wave tank, Ocean Eng. 75 (2014) 165–173.
[27] A. Karperaki, T. Papathanasiou, K. Belibassakis, An optimized, parameter-free PML-FEM for wave scattering problems in the ocean and coastal environment, Ocean Eng. 179 (2019) 307–324.